

Isotope effects on transport in LHD

メタデータ	言語: eng 出版者: 公開日: 2022-06-01 キーワード (Ja): キーワード (En): 作成者: TANAKA, Kenji, NAGAOKA, Kenichi, IDA, Katsumi, YAMADA, H., KOBAYASHI, Tatsuya, SATAKE, Shinsuke, NAKATA, Motoki, KINOSHITA, Toshiki, OHTANI, Yoshiaki, TOKUZAWA, Tokihiko, TAKAHASHI, Hiromi, WARMER, Felix, MUKAI, Kiyofumi, MURAKAMI, Sadayoshi, SAKAMOTO, Ryuichi, NAKANO, Haruhisa, OSAKABE, Masaki, MORISAKI, Tomohiko, NUNAMI, Masanori, TALA, T., TSUJIMURA, Toru, TAKEMURA, Yuki, YOKOYAMA, Masayuki, SEKI, Ryosuke, IGAMI, Hiroe, YOSHIMURA, Yasuo, KUBO, Shin, SHIMOZUMA, Takashi, AKIYAMA, Tsuyoshi, YAMADA, Ichihiro, YASUHARA, Ryo, FUNABA, Hisamichi, YOSHINUMA, Mikiro, GOTO, Motoshi, OISHI, Tetsutarou, MORITA, Shigeru, MOTOJIMA, Gen, SHOJI, Mamoru, MASUZAKI, Suguru, MICHAEL, Clive A., VACHESLAVOV, L. N. メールアドレス: 所属:
URL	http://hdl.handle.net/10655/00013181

This work is licensed under a Creative Commons Attribution 3.0 International License.

PAPER • OPEN ACCESS

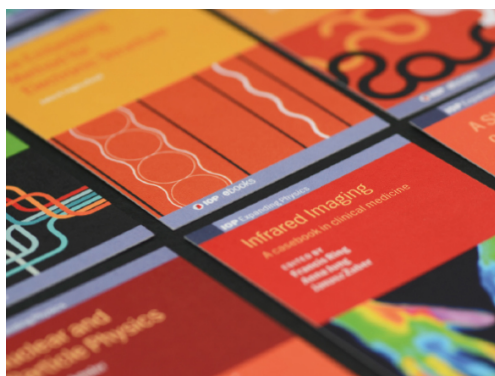
Isotope effects on transport in LHD

To cite this article: K Tanaka *et al* 2021 *Plasma Phys. Control. Fusion* **63** 094001

View the [article online](#) for updates and enhancements.

You may also like

- [Particle transport of electron cyclotron resonant heating plasma in Large Helical Device](#)
Yoshiaki Ohtani, Kenji Tanaka, Tokihiko Tokuzawa *et al*.
- [Improvement in the heating efficiency of fast ignition inertial confinement fusion through suppression of the preformed plasma](#)
Y. Arikawa, S. Kojima, A. Morace *et al*.
- [Effects of reconnection downstream conditions on electron parallel acceleration during the merging start-up of a spherical tokamak](#)
M. Inomoto, T. Ushiki, X. Guo *et al*.



IOP | ebooks™

Bringing together innovative digital publishing with leading authors from the global scientific community.

Start exploring the collection—download the first chapter of every title for free.

Isotope effects on transport in LHD

K Tanaka^{1,2,*} , K Nagaoka^{1,3} , K Ida^{1,4} , H Yamada⁵, T Kobayashi^{1,4}, S Satake^{1,4} , M Nakata^{1,4} , T Kinoshita² , Y Ohtani⁶ , T Tokuzawa^{1,4}, H Takahashi^{1,4}, F Warmer⁷, K Mukai^{1,4}, S Murakami⁸, R Sakamoto^{1,4}, H Nakano^{1,4}, M Osakabe^{1,4}, T Morisaki^{1,4} , M Nunami^{1,4}, T Tala⁹, T Tsujimura^{1,4}, Y Takemura^{1,4}, M Yokoyama^{1,4}, R Seki^{1,4}, H Igami¹, Y Yoshimura¹, S Kubo^{1,3}, T Shimozuma¹, T Akiyama^{1,**}, I Yamada¹, R Yasuhara^{1,4}, H Funaba¹, M Yoshinuma¹, M Goto^{1,4}, T Oishi^{1,4}, S Morita^{1,4}, G Motojima^{1,4}, M Shoji¹, S Masuzaki^{1,4}, C A Michael¹⁰ and L N Vacheslavov^{11,12}

¹ National Institute for Fusion Science, National Institutes of Natural Sciences, Toki, Gifu 509-5292, Japan

² Kyushu University, Department of Advanced Energy Engineering, Kasuga, Fukuoka 816-8580, Japan

³ Nagoya University, Graduate School of Science, Nagoya 464-8601, Japan

⁴ SOKENDAI (The Graduate University for Advanced Studies), Toki, Gifu 509-5292, Japan

⁵ Graduate School of Frontier Sciences, The University of Tokyo, Kashiwa 277-8561, Japan

⁶ Naka Fusion Institute, National Institutes for Quantum and Radiological Science and Technology, 801-1, Mukoyama, Naka, Ibaraki 311-0193, Japan

⁷ Max-Planck-Institut für Plasmaphysik, Greifswald, Germany

⁸ Department of Nuclear Engineering, Kyoto University, Kyoto 615-8510, Japan

⁹ VTT, P.O. Box 1000, FI-02044 VTT Espoo, Finland

¹⁰ University of California-Los Angeles, Los Angeles, CA, United States of America

¹¹ Budker Institute of Nuclear Physics, 630090 Novosibirsk, Russia

¹² Novosibirsk State University, Novosibirsk 630090, Russia

E-mail: ktanaka@nifs.ac.jp

Received 31 December 2020, revised 31 March 2021

Accepted for publication 10 May 2021

Published 26 July 2021



Abstract

Isotope effects are one of the most important issues for predicting future reactor operations. Large helical device (LHD) is the presently working largest stellarator/helical device using super conducting helical coils. In LHD, deuterium experiments started in 2017. Extensive studies regarding isotope effects on transport have been carried out. In this paper, the results of isotope effect studies in LHD are reported. The systematic studies were performed adjusting operational parameters and nondimensional parameters. In L mode like normal confinement plasma, where internal and edge transport barriers are not formed, the scaling of global energy confinement time (τ_E) with operational parameters shows positive mass dependence ($M^{0.27}$; where M is effective ion mass) in electron cyclotron heating plasma and no mass dependence ($M^{0.0}$) in neutral beam injection heating plasma. The non-negative ion mass dependence is anti-gyro-Bohm scaling. The role of the turbulence in isotope effects was also found by turbulence measurements and gyrokinetic simulation. Better accessibility to electron and ion internal transport barrier (ITB) plasma is found in deuterium (D) plasma than in hydrogen (H). Gyro kinetic non-linear simulation shows reduced ion heat flux due to the larger generation of

* Author to whom any correspondence should be addressed.

** Present address: General Atomics, San Diego, CA, United States of America



Original Content from this work may be used under the terms of the [Creative Commons Attribution 4.0 licence](https://creativecommons.org/licenses/by/4.0/). Any further distribution of this work must maintain attribution to the author(s) and the title of the work, journal citation and DOI.

zonal flow in deuterium plasma. Peaked carbon density profile plays a prominent role in reducing ion energy transport in ITB plasma. This is evident only in plasma with deuterium ions. New findings on the mixing and non-mixing states of D and H particle transports are reported. In the mixing state, ion particle diffusivities are higher than electron particle diffusivities and D and H ion density profiles are almost identical. In the non-mixing state, ion particle diffusivity is much lower than electron diffusivity. Deuterium and hydrogen ion profiles are clearly different. Different turbulence structures were found in the mixing and non-mixing states suggesting different turbulence modes play a role.

Keywords: isotope effect, turbulence, transport, stellarator, heliotron, gyrokinetic simulation

(Some figures may appear in color only in the online journal)

1. Introduction

The isotope effect on transport is one of the un-resolved important issues in fusion research. Understanding the isotope effect is essential to predict the performance of the deuterium (D) and tritium (T) fusion reactor from the present database, where deuterium and hydrogen (H) are used for the fueling species. In a tokamak, better confinement characteristics together with lower H mode threshold power have been reported [1–8]. The reduced transport in D plasma is in contradiction to the gyro-Bohm diffusion, where ion scale turbulence such as ion temperature gradient mode (ITG) and trapped electron mode (TEM) play roles in transport. Many global energy scalings show gyro-Bohm dependence except ion mass. In the gyro-Bohm diffusion process, the wavelength of the ion scale turbulence is on the order of the ion Larmor radius. The step size of the diffusion process and the diffusion coefficient are described as follows [9]:

$$\chi_{\text{Gyro Bohm}} \propto \rho^* \chi_{\text{Bohm}} = \frac{M^{0.5} T^{1.5}}{aq^2 B^2} \quad (1)$$

here, ρ^* is the normalized ion Larmor radius ($\rho^* = \rho_i/a$, $\rho_i = \sqrt{TM/qB}$, ρ_i : ion Larmor radius), M is ion mass, T is ion temperature, a is plasma minor radius, q is ion charge and B is magnetic field. $\chi_{\text{Bohm}} \propto T/qB$ is the Bohm diffusion coefficient. In Bohm diffusion, the long wavelength turbulence, with wavelengths on the order of the scale lengths of the density or temperature gradient, plays a role in the diffusion process. In gyro-Bohm diffusion, the global energy confinement (τ_E) time is given by $\tau_E \sim \int nT dV/P \sim a^2/\chi$, where n is plasma density, V is plasma volume, P is heating deposition power, and χ is thermal conductivity. Then, τ_E governed by gyro-Bohm diffusion is expressed as follows [3]:

$$\tau_{E \text{ Gyro Bohm}} \propto a^3 B^{0.8} n^{0.6} P^{-0.6} M^{-0.2}. \quad (2)$$

Tokamak scaling laws [1, 2, 10] show close to gyro-Bohm dependence except ion charge and ion mass number. These scalings show positive ion mass dependence against gyro-Bohm diffusion. One of the contradictions and mysteries is that global confinement is anti-gyro-Bohm, although the linear growth rate of ITG and TEM shows gyro-Bohm nature.

There is significant progress in theoretical work to understand anti-gyro-Bohm characteristics. These are the stronger stabilization effects on the ion scale turbulence due to the radial electric field (E_r) shear in heavier ion mass plasma [11], stronger collisionality effects of turbulence saturation in TEM [12, 13], and nonadiabatic response associated with fast electron parallel motion [14]. Validation with experimental observations have been performed [15–18]. Early validation studies using gyrokinetic simulations with collisionless assumption showed discrepancy from the experimental observation as the gyrokinetic nonlinear simulation underestimated the heat flux in H plasma [15, 16]. However, the recent validation studies in JET H and D plasma of the ELMy H mode show reasonable agreement between experimental heat flux and heat flux predicted by gyrokinetic simulation taking into account collision effects, ExB shear from bulk toroidal rotation and dilution due to Beryllium ions [17, 18]. Taking into account the uncertainty of electron temperature (T_e), and ion temperature (T_i) profile measurements, 20% lower normalized temperature gradients were inputted to the gyrokinetic nonlinear simulation. Simulated heat flux then almost agreed with experimental observation [18]. In addition, the fast ion pressure can stabilize ITG turbulence and cause isotope effects [18, 19]. Taking into account these effects, the experimentally observed anti-Gyro-Bohm characteristics are well explained in tokamak core plasma of ELMy H mode [18]. On the other hand, the physics mechanism of isotope effects in the edge pedestal in tokamaks are still under investigation and clear physics mechanism are not yet explained [18].

Limited data sets of isotope experiments were reported in stellarator/heliotron devices before large helical device (LHD) experiments [20–22]. The international stellarator scaling 2004 (ISS04) [23] shows gyro-Bohm parameter dependence on n , a , B and P . However, ion charge and mass dependence were not shown because the database was hydrogen plasma only. LHD deuterium experimental campaign was started in 2017. Extensive studies of isotope effects have been carried out. In LHD, a variety of heating schemes is available. The electron cyclotron resonant heating (ECRH) system consists of five sets of gyrotrons—three 77 GHz, two 154 GHz. The power of each gyrotron is ~ 1 MW. The neutral beam injection consists of three negative ion-based neutral beams (NNB) and two positive ion-based neutral beams (PNB). The negative

ion-based neutral beams are injected tangentially to the magnetic field and their injection power is ~ 5 MW each in hydrogen and ~ 3 MW each in deuterium. The positive ion-based neutral beams are injected perpendicularly to the magnetic field and their injection power is ~ 5 MW each in hydrogen and ~ 8.5 MW each in deuterium [25]. The positive ion based neutral beam predominantly heats ion. On the other hand, and the negative ion based neutral beam predominantly heats electron. The different heating channels are due to the difference in injection energies. The injection energy of PNBs is 40 keV in H plasma and 60 \sim 80 keV in D plasma. The injection energy of the PNB is lower than the critical energy [24–26]. On the other hand, the injection energy of NNBs is 180 keV both in H and D plasma. The injection energy of the NNB is higher than the critical energy [24–26].

These heating schemes enable the construction of a database of isotope experiments scanning a wide range of plasma parameters.

The isotope experiments in LHD show a clear view of isotope effects in stellarator/heliotron devices for the first time. According to a recent theoretical study, the isotope effects of neoclassical transport are weak in electron root and negligibly small in ion root [27]. Thus, observed isotope effects originate from the turbulence-driven anomalous effects also seen in a tokamak. In addition to a difference in magnetic properties, the different profile shapes in LHD and tokamak provide opportunities to examine the theoretical model of isotope effects. In particular, temperature ratio (T_e/T_i) in NB heated plasma and density profiles are clearly different in LHD and tokamak. In LHD, NNBs heat electrons predominantly, then, $T_e/T_i > 1$ can be achieved in the entire region of the plasma. On the other hand, in tokamak, T_e/T_i is generally equal or larger than 1, since NBs in most of tokamak are PNB and heat ions predominantly. Density profiles in LHD are hollowed in many cases both in ECRH and NB heated plasma due to the neoclassical thermo-diffusion [28, 29]. This is in strong contrast to the tokamak, where density profiles are generally peaked [30] except for strong central ECRH heating [31]. The temperature ratio and density gradients play important roles in turbulence stabilities and saturation mechanisms. These characteristics of profiles result in finding a new aspect of isotope effects in toroidal devices.

Most of the contents in this paper are based on published material. Some new data are added to support reported results. New data include evaluations of scaling from kinetic τ_E in ECRH plasma, while diamagnetic τ_E were used in the previous studies [32], the isotope effects of ion scale turbulence in dimensionally similar plasmas, and the isotope effects of transition to electron-ITB in high density region. Particle transports have been extensively investigated by recently performed density modulation experiments. The results are reported in a separate publication [33]. The following is the structure of this publication. In section 2, isotope effects of ECRH plasma are reported. In ECRH plasma, electron density and heating power were scanned to evaluate τ_E scaling. Also, transport and turbulence characteristics are compared, adjusting operational parameters. In section 3, isotope effects of NNB heated plasma

are reported. The dimensionless parameters, which are normalized ion Larmor radius (ρ^*), normalized collisionality (ν^*) and normalized pressure (β) are adjusted identically in H and D plasmas. Optimal adjustments are achieved by tuning density and heating power at different magnetic field, in H at 1.64 T and in D at 2.75 T. In section 4, isotope effects in the internal transport barrier (ITB) are reported. In section 5, the particle transports in hydrogen–deuterium mixed plasma are reported. Finally, a summary and discussion are given in section 5. The magnetic configuration of the experimental results in this paper is the so-called inward-shifted configuration except for some data points in figure 14 about the the configuration dependence of isotope effects. The inward-shifted configuration has a magnetic axis position (R_{ax}) of 3.6 m and shows the best performance in the data set of the ISS04 scaling study [23].

2. Isotope effects of ECRH plasma on adjusting operational parameters

ECRH is a promising heating technique to control electron temperature profiles. Due to the good accessibility to the plasma, ECRH will be the main heating technique in future reactors. The discharges described in this section are heated by ECRH only. The PNB was injected for charge exchange recombination spectroscopy (CXRS) with a shot pulse (20 ms pulse width every 400 ms step) but this does not contribute any ion heating. The ion heating is due to the electron–ion energy equipartition only.

The results reported in this section are from ECRH plasma tangentially injected in a horizontal port [34]. Perpendicular injection was not performed in order to avoid damage to diverter cryo-pumps, which are located on the inner torus side. The plasma current induced by the tangentially injected ECRH affects the profiles of rotational transform and magnetic topologies. These effects bring additional effects on transport in addition to isotope effects [35–38]. In order to investigate the isotope effects in ECRH plasma clearly, the effects of plasma current induced by tangentially injected ECRH were minimized using balanced injections. The magnetic field was set to be 2.75 T for the 77 GHz fundamental and 154 GHz second harmonic heating. The problem of tangential injection is the refraction effect due to the long distance from the resonance layer. Part of the refracted microwave transmits through the plasma without absorption. Such microwaves are reflected at the vacuum vessel and returns to the plasma again. Such multiple injections make the deposition profile very uncertain. Therefore, 77 GHz fundamental heating was used in low density only (line-averaged density n_e bar $< 1.6 \times 10^{19} \text{ m}^{-3}$), where refraction is negligible. On the other hand, the refraction effect of 154 GHz is negligible in the whole dataset, where n_e bar $< 5 \times 10^{19} \text{ m}^{-3}$. Thus, 154 GHz were used in the whole data set with balanced injection. Also, focusing positions were carefully set to be identical in both H and D plasma. This is because a small difference in the focusing spot results in a large difference in performance.

In the 21st LHD experimental campaign in 2019–2020, data sets of kinetic τ_E of ECRH plasma were obtained. In the previous study [32], τ_E was estimated using diamagnetic stored energy due to the lack of ion temperature (T_i) profiles. The kinetic stored energy was estimated from electron density (n_e), electron temperature (T_e) profiles by Thomson scattering [39], and ion temperature profiles by CXRS [40]. The ion density ratio between H and D was estimated from the $H\alpha$ and $D\alpha$ intensities. The contamination with He was evaluated by the ratios of calibrated HeI , $H\alpha$ and $D\alpha$ line intensities [41]. These neutral atom line intensities are generally thought to stand for the neutral fluxes at the plasma edge. Here we assume that the neutral flux approximately represents the ion density in the plasma and the ion ratio is constant in space. In the data set, the purity of H and D are close to 100%, where $n_D/(n_H + n_D) \sim 0$ in H plasma and $n_D/(n_H + n_D) \sim 1$ in D plasma. n_H and n_D are the hydrogen and deuterium ion density. There is about 5%–10% He contamination in the total ion density. The helium contamination is due to residual components of helium discharge cleaning. The following scaling law was deduced from the database and figure 1 shows scaling from this data set:

$$\tau_E = 0.096 M^{0.27 \pm 0.03} \bar{n}_e^{0.57 \pm 0.01} P_{abs}^{-0.74 \pm 0.04} \quad (3)$$

here M is the effective ion mass, \bar{n}_e is the line averaged density and P_{abs} is the absorption power. The value of M was estimated from the ratio of three ion species (H, D, He). The effective ion mass was 1.3 ± 0.1 in H plasma and 2.1 ± 0.1 in D plasma. In the data set, B was fixed at 2.75 T and the configuration was fixed at $R_{ax} = 3.6$ m, thus, plasma size (major and minor radius) was fixed. In the data set of figure 1, \bar{n}_e was scanned over approximately $0.4\text{--}4.9 \times 10^{19} \text{ m}^{-3}$ in H plasma and $0.6\text{--}4.7 \times 10^{19} \text{ m}^{-3}$ in D plasma. The deposition power was scanned over the range of about 1.4–2.2 MW both in H and D plasma. The deposition of the first path absorption was estimated by using LHDGAUSS [42] and was higher than 95% both in H and D plasma. Thus, the effect of multiple reflection of un-absorbed power is negligible. Equation (3) shows clear positive ion mass effects, which are anti-gyro-Bohm. Compared with the Gyro-Bohm scaling of equation (2), the density dependence is comparable and the power dependence is slightly stronger. Compared with ISS04 [23], the density dependence is comparable and the power dependence is slightly stronger.

Figure 2 shows the collisionality dependence of kinetic τ_E . The normalized collisionality in figure 2 is defined as $\nu_h^* = \nu_{ei}/(\varepsilon_{eff}^{3/2} v_T/qR_{mj})$. ν_{ei} is the electron ion collision frequency, v_T is the electron thermal velocity, q is the safety factor, R_{mj} is the major radius, and ε_{eff} is an effective helical ripple [28, 43, 44]. $\nu_h^* = 1$ is the boundary between $1/\nu$, where neoclassical coefficients are inversely proportional to collisionality, and the plateau regime. As shown in figure 2, τ_E increases with increasing ν_h^* . However, the increase saturates at $\nu_h^*(\rho = 0.5) \sim 0.6$. The isotope effects are different depending on ν_h^* . At $\nu_h^*(\rho = 0.5) < 0.6$, a difference in τ_E is not apparent between H and D. At $\nu_h^*(\rho = 0.5) = 0.6 \sim 6$, the difference in τ_E becomes clearer. At $\nu_h^*(\rho = 0.5) > \sim 6$, again,

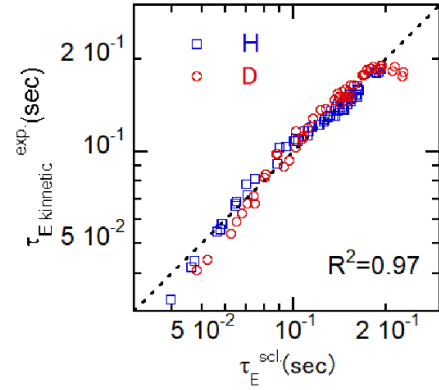


Figure 1. Comparison of the thermal energy confinement time in the experiment and the prediction by the scaling of ECRH plasma. Squares and circles are hydrogen plasmas and deuterium plasmas, respectively. R^2 is the correlation coefficients of the scaling.

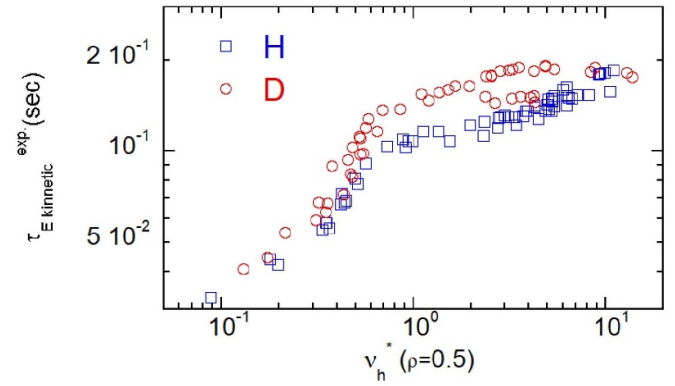


Figure 2. Collisionality dependence of τ_E in ECRH plasma of LHD.

the difference in τ_E becomes smaller. The results suggest that isotope effects are different depending on collisionality.

According to local power balance analyses by TASK3D [45], the electron thermal conductivities χ_e are almost identical in the low collisionality regime [46]. On the other hand, in the high collisionality regime, clear differences of transport are found [46]. Figure 3 shows comparison of the profiles in the high collisionality case. The line-averaged density was $3 \times 10^{19} \text{ m}^{-3}$ and injection power was 154 GHz 2 MW ECRH with balanced injection in both cases. As shown in figure 3(a), T_e is clearly higher in D plasma, while T_i is almost identical. The electron density profiles are more hollowed in D plasma. The 3D Monte Carlo simulation EIRINE [47] shows the peak of the edge particle source has a peak at $\rho = 1.05$ and it decreases exponentially toward the plasma core [32]. The penetration of hydrogen atoms is deeper due to the lighter ion mass. However, the difference is negligible [32]. The small difference of the particle source does not cause the difference in density profile. Also, the difference in carbon impurity does not play a role in the observed difference of the n_e profile [32]. The isotope effects of neoclassical transport are negligibly small, in particular in the neoclassical ion root, which is the case of figure 3. However, higher T_e in

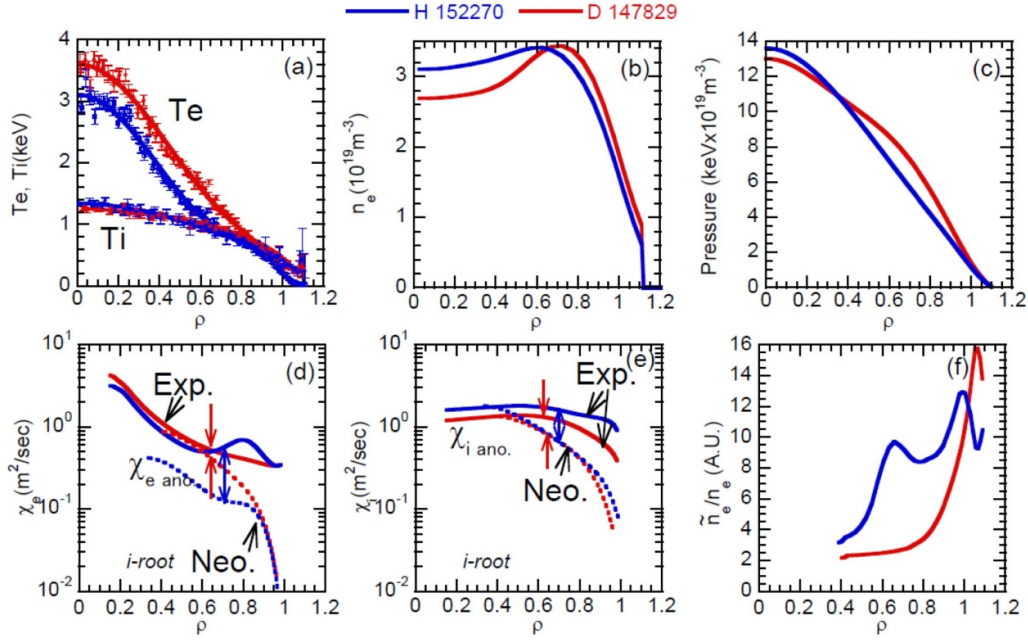


Figure 3. Profiles in high density (a) T_e , T_i , (b) n_e , (c) pressure, (d) χ_e , (e) χ_i , and (f) turbulence level. In (d) and (e), χ_e and χ_i from power balance analyses are shown by solid lines and , from neoclassical estimations by dashed lines [46]. Reproduced from [46]. © IOP Publishing Ltd All rights reserved.

D plasma enhances neoclassical convection, which is mainly neoclassical thermo-diffusion. This makes density profiles hollower in D plasma. The previous studies showed experimental estimated convection velocities are comparable with neoclassical values [28, 29]. Thus, higher neoclassical convection and lower anomalous diffusion in D plasma result in hollower density profiles in D plasma. More detail investigations about the isotope effects on particle transport will be reported in [33].

One of the particularities of ECRH plasma is equipartition heating. The ion heating is due to energy equipartition. The power of the equipartition heating is given by the following equation [9]:

$$P_{ei} \propto \frac{Z_i^2 n^2}{m_i T_e^{3/2}} (T_e - T_i) \quad (4)$$

here Z_i is ion charge number, n is electron density, m_i is ion mass, and T_e and T_i are electron and ion temperature. As shown in equation (4), due to the inverse ion mass dependence, P_{ei} doubles in H plasma for same density and temperature difference. Thus, higher P_{ei} in H plasma results in lower electron heating power (P_e), where $P_e = P_{total} - P_{ei}$, and P_{total} is total deposition power. The higher T_e in D plasma as shown in figure 3(a) can be interpreted to be caused by partly higher P_e in D plasma. The ratio of χ_e between H and D plasma at $\rho < 0.8$, where T_e is clearly higher in D plasma, is comparable with the ratio of T_e . However, it should be noted that the χ_e ratio is clearly lower than the Gyro-Bohm prediction by equation (1) using T_e .

As shown in figure 3(d), at $\rho < 0.8$, $\chi_{e, neo}$, which is the neoclassical electron thermal conductivity, becomes comparable with χ_e from power balance analyses. This suggests that the

contribution of anomalous transport reduces at this location, where the turbulence level is clearly lower in D plasma than in H plasma as shown in figure 3(f). The ion thermal conductivity is lower in D plasma in the entire region as shown in figure 3(e). Ion heating power is higher in H plasma than D plasma. However, the resultant T_i profiles are almost identical in H and D plasma as shown in figure 3(a). Thus, both total χ_i and anomalous χ_i in D plasma become lower in D plasma. The ion scale turbulence measured by two-dimensional phase contrast imaging (2D-PCI) [48, 49] shows a clear reduction of turbulence level as shown in figure 3(f). The reduction is observed in almost the entire region. Thus, the reduction of the turbulence in D plasma is suggested to contribute to the reduced anomalous transport in both the electron and ion channel.

In ASDEX-U L mode ECRH plasma, ion and electron energy transports were compared in H and D plasma [6]. The same transport model without ion mass dependence can reproduce the experimental χ_e and χ_i [6]. Thus, there is no improvement of the confinement in D plasma compared with H plasma [6]. The ASDEX-U has a tungsten wall. However, the effective ion charge number (Z_{eff}) is around 1 in both H and D plasma of L mode ECRH [6]. In LHD, the divertor plate is carbon and the main impurity is carbon. Z_{eff} is around 1.3 in H plasma and 1.5 in D plasma. Higher Z_{eff} in D plasma is due to the higher C^{6+} density. It should be noted that Z_{eff} is almost identical in the low ($\sim 1.6 \times 10^{19} \text{ m}^{-3}$) and high density ($\sim 3 \times 10^{19} \text{ m}^{-3}$) regime, while electron transport and turbulence is clearly reduced only in the high density regime. The impurity ions can stabilize ITG turbulence [50]. However, the reason for the reduced turbulence and transport in high density D plasma is not due to the higher impurity density. The effects of impurity ions on turbulence and transport will be reported in ref. [33].

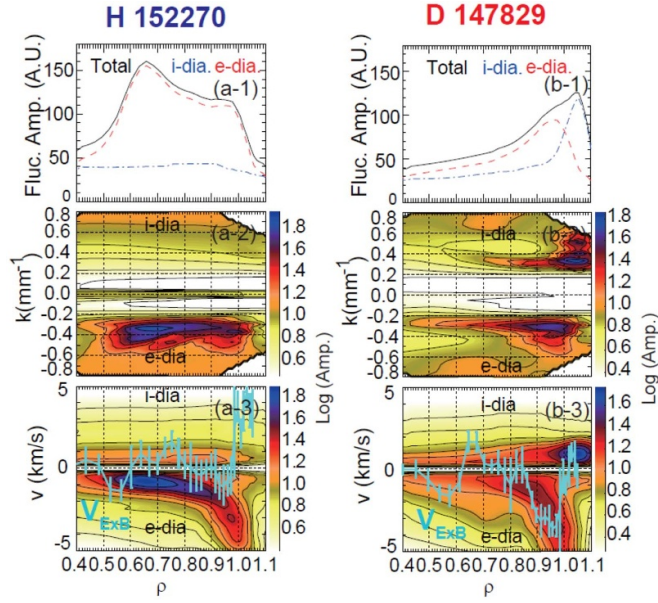


Figure 4. Spatial profiles of high density case (a-1), (b-1) turbulence amplitude, (a-2), (b-2) wavenumber spectrum and (a-3), (b-3) turbulence phase velocity. In (a-3) and (b-3), V_{ExB} measured by CXRS is shown by the blue line [46]. Reproduced from [46]. © IOP Publishing Ltd All rights reserved.

Figure 4 shows a comparison of turbulence spatial structure. In figure 4, spatial profiles of turbulence amplitude (a-1), (b-1), wavenumber spectra (a-2), (b-2) and turbulence phase velocities are shown. These quantities are not normalized by background electron density. 2D-PCI measures turbulence of which the frequency is 20–500 kHz and the wavenumber is $k = 0.1\text{--}0.8\text{ mm}^{-1}$. The accessible region is $\rho > 0.4$. The vertical injection of the probe laser beam can measure the upper side and the lower side relative to the equatorial plane [32]. The measured wavenumber is poloidally dominated. In figure 4, ion diamagnetic direction (i-dia) and electron diamagnetic direction (e-dia) indicate the propagation direction of turbulence in the laboratory frame. In figures 4(a-3) and (b-3), ExB poloidal rotation velocities (V_{ExB}) are shown by blue lines.

As shown in figures 4(a-1) and (b-1), turbulence amplitude profiles are clearly different. The turbulence amplitude is higher in H plasma than in D plasma except close to the plasma boundary. Turbulence expands in the more inner region in H plasmas. This amplitude profile results in a reduced fluctuation level as shown in figure 3(f). As shown in figures 4(a-2) and (b-2), measured k is $k \sim 0.3\text{ mm}^{-1}$. Although absolute k is a similar value, normalized k becomes different. The wavenumber normalized by ion Larmor radius ($k\rho_i$) is approximately 0.33–0.36 in H plasma and 0.4–0.51 in D plasma. As shown in figure 4(a-3), most of the components propagate toward the e-dia direction in laboratory frame in H plasma, and the phase velocity is further toward the e-dia direction compared with V_{ExB} at $\rho = 0.6\text{--}0.8$ in H plasma. This observation indicates that the turbulence propagates toward the e-dia direction in plasma frame of H plasma. While in D plasma, as shown in figure 4(b-3), the turbulence propagation direction changes from e-dia direction to i-dia direction at about $\rho = 0.95\text{--}1.05$. The turbulence phase velocities follow V_{ExB} . As shown in

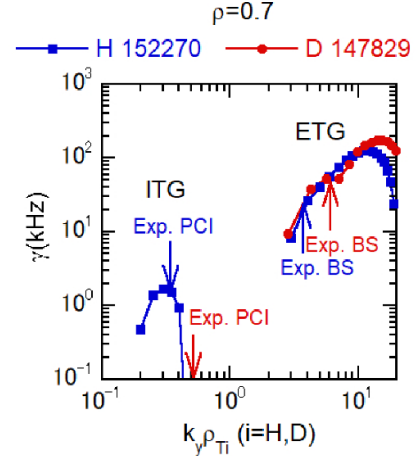


Figure 5. Linear spectrum of growth rate (γ) at $\rho = 0.7$ case (H 152270, D 147829). $k_y \rho_i$ is the normalized wavenumber, where ρ_i is ion Larmor radius. ρ_i is calculated for hydrogen and deuterium ion mass respectively. The measured $k_y \rho_i$ are shown by the arrows [46]. Adapted from [46]. © IOP Publishing Ltd All rights reserved.

figure 4, not only amplitude, but also spatial structures are clearly different in H and D plasma.

Figure 5 shows the linear spectrum at $\rho = 0.7$ of figure 4 by local flux tube gyro kinetic simulation GKV code [51, 52]. Input parameters are shown in table 1. The dominant mode of ion scale turbulence is ITG. As shown in figure 5, ITG is stabilized in D plasma. This result qualitatively agrees with the reduced turbulence level observed experimentally in D plasma as shown in figure 3(f). However, the lower growth rate is not due to the difference of ion mass, but due to the difference of profile. As shown in table 1, R/L_n and R/L_{ti} are lower and R/L_{te} are higher in D plasma. The largest difference is R/L_n , which corresponds to hollower density profiles in D plasma than in H plasma. The growth rate of electron temperature gradient mode is comparable in H and D plasma. The measurements of microwave backward scattering (BS) [53] showed a higher turbulence level in the unstable ETG wavenumber region [32]. The growth rate of ETG is much higher than that of ITG. However, higher growth rate of the ETG does not indicate a higher contribution to electron transport. This is because a higher k corresponds to a smaller step size of the turbulence driven diffusion and diffusion coefficients becomes much smaller for higher k . ETG plays a role in transport when a radial streamer is formed. Recent gyrokinetic study shows that negative shear of the safety factor breaks streamers [54]. This is the case of a negative shear tokamak, W-7X and LHD. Non-linear simulations are necessary for the quantitative arguments for the ETG.

One contradiction between turbulence measurements and gyrokinetic calculation is propagation direction. As shown in figure 4(a-3), turbulence propagates toward the e-dia direction in the plasma frame at $\rho = 0.6\text{--}0.8$. This is against the basic characteristics of ITG, which propagates toward the i-dia direction in the plasma frame. Other types of instabilities should also be considered. The turbulence level at about $\rho = 0.5\text{--}0.8$ increases with increase of collisionality

Table 1. Input parameters of linear calculation [46].

ion	Shot	R/L_n	R/L_{te}	R/L_{ti}	T_e/T_i	ITG	ETG
H	152 270	2.91	13.44	8.31	1.05	Unstable	Unstable
D	147 829	−0.68	16.7	6.05	1.34	Stable	Unstable

at $\nu^*h > 4$ [32]. Dissipative trapped electron mode (DTEM) can increase the growth rate with increase of collisionality at ν^*h ($\rho = 0.5\text{--}0.8$) > 4 and qualitatively agree with observation in LHD. However, according to the analytical theory, DTEM appears in the very low collisionality regime only [9], although there is a report of DTEM from the Advanced Toroidal Facility (ATF), which is a similar magnetic configuration to LHD [55]. The resistive interchange (RI) turbulence [56] is another candidate to explain the observations in LHD. Its growth rate increases with increase of resistivity and approximately with increase of collisionality. The propagation direction is the e-dia direction in the plasma frame. In high beta plasma of LHD, turbulence level measured by a far-infrared laser interferometer increases with increase of β corresponding to increase of collisionality suggesting that RI turbulence degrades the transport [57]. Unfortunately, RI mode cannot be calculated by using present gyrokinetic code, since the parallel wavenumber of RI is zero and its eigen function is not ballooning structure. It will be possible to investigate RI mode using MHD fluid code. Then, the role of RI turbulence in isotope effects can be investigated.

3. Isotope effects of neutral beam injection (NBI) heated plasma by adjusting nondimensional parameters

The isotope effects were investigated for the NNB heating plasma as well. The scaling study including isotope effects was performed scanning density, heating power and magnetic fields [58]. The line-averaged density was scanned over the approximate range of $0.64\text{--}4.32 \times 10^{19} \text{ m}^{-3}$ in H and $0.64\text{--}5.7 \times 10^{19} \text{ m}^{-3}$ in D plasma. The absorption powers of the NNB are about 1.8–11.7 MW in H and 1.5–12.5 MW in D plasma. It should be noted that the plasmas investigated are under electron dominant heating since high energy (180 keV) NNB is the heating source. The ion species of NNB are hydrogen both in H and D plasma. However, since beam fueling due to the NNB is small, the purity of H and D achieved was more than 90% both in H and D plasma. PNB was used for the CXRS measurements with a short pulse (20 ms) and did not contribute to the ion heating. The magnetic fields were 1.64 and 2.75 T in H and 1.375 and 2.75 T in D plasma. The datasets consisted of 64 cases in H and 103 cases in D plasma. The following scaling law was deduced from the database and figure 6 shows comparison of experiment data with prediction by the scaling:

$$\tau_{E,th}^{scl} = 0.072 M^{0.00 \pm 0.02} B^{0.84 \pm 0.02} \bar{n}_e^{0.76 \pm 0.01} P_{abs}^{-0.87 \pm 0.01}. \quad (5)$$

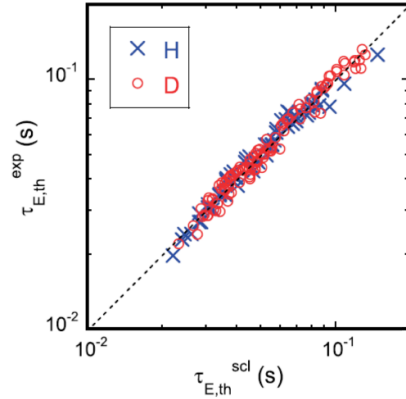


Figure 6. Comparison of the thermal energy confinement time in the experiment and the prediction by the scaling of dimensionally similar NBI plasma. Crosses and circles are hydrogen plasmas and deuterium plasmas, respectively [58]. Reprinted figure with permission from [58]. Copyright (2019) by the American Physical Society.

Equation (5) does not show any ion mass effects. Compared with the gyro-Bohm scaling of equation (2), the magnetic field dependence is comparable, the density dependence is stronger, and power dependence is slightly stronger. Compared with ISS04 [23], the magnetic field dependence is identical, the density dependence is stronger and power dependence is slightly stronger. The data base of ISS04 from LHD is from hydrogen NNB heated plasma. However, the maximum injection power was about 6 MW. Here the maximum injection power is about 12 MW. The stronger power degradation becomes evident by using higher heating power. Compared with the scaling of ECRH plasma in equation (3), density and power dependences are slightly stronger. However, a noticeable difference is ion mass dependence, which is $M^{0.27}$ in ECRH plasma.

Among the data sets of the scaling study, 12 pairs adjusting ρ^* , ν^* and β in H and D plasmas were available. The set of plasmas with identical nondimensional parameters (ρ^* , ν^* and β) are considered to be governed by identical transport physics [59, 60]. Such plasmas are called dimensionally similar plasma. Identical normalized confinement time and transport coefficients are reported from the data set of different size and different operational regime of dimensionally similar plasma [59]. These experimental results support the expectation that plasmas with the same dimensionless parameters are subject to the same physics processes. This experimental technique is particularly useful to predict the performance of a future large-scale reactor from the dataset of the current working machine [61], although reactor relevant ρ^* , ν^* and β have not been achieved simultaneously under the present conditions.

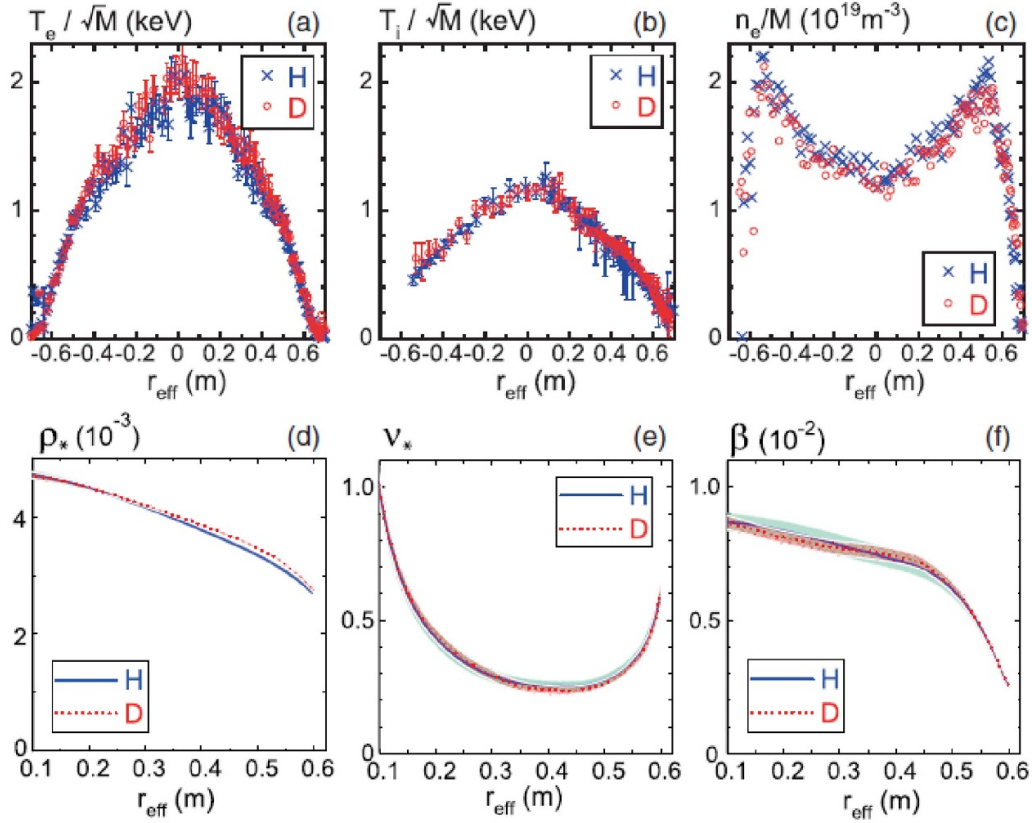


Figure 7. Profiles of dimensionally similar hydrogen and deuterium plasmas. r_{eff} is the effective minor radius, and the last closed flux surface is located at $r_{\text{eff}} = 0.63$ m. The negative and positive signs mean the inboard side and the outboard side with respect to the magnetic axis, respectively. (a) The electron temperature, (b) ion temperature, and (c) electron density in the top panels. Data from hydrogen plasma and deuterium plasma are shown by crosses and circles, respectively. (d) The normalized gyroradius, (e) normalized collisionality, and (f) normalized pressure in the bottom panels. Data from hydrogen plasma and deuterium plasma are shown by solid and dashed curves, respectively [58]. Reprinted figure with permission from [58]. Copyright (2019) by the American Physical Society.

The application of dimensionally similar experiments to the isotope experiments examines different features. If the normalized confinement time or normalized transport coefficients are identical for dimensionally similar plasma of H and D, transport follows an identical physics story. The examined transport model in this study is gyro-Bohm diffusion.

First, the scaling of operational parameters shown by equation (5) are rephrased by using ρ^* , ν^* and β . Here, the global energy confinement time is normalized by the ion cyclotron frequency (Ω_i). The normalized global energy confinement time $\tau_E \Omega_i$ is proportional to ρ^{*-2} in Bohm diffusion and proportional to ρ^{*-3} in gyro-Bohm diffusion. Thus, the ρ^* dependence in power law scaling can indicate that scaling is governed by Bohm or gyro-Bohm. The following scaling law was obtained from the data set of dimensionally similar plasma:

$$\tau_E \Omega_i \propto M^{0.99} \rho^{*-3} \nu^{*0.19} \beta^{-0.30}. \quad (6)$$

Then, local analyses were carried out for the pairs of identical ρ^* , ν^* and β . In order to adjust the ρ^* , ν^* and β values, the ratio of magnetic field, density and temperature between D and H plasmas should be adjusted to be $M^{3/4}$, M , and \sqrt{M} , respectively. Here M is ion mass ratio of D plasma to H plasma. For

pure H ($M = 1$) and D ($M = 2$), in D plasma, these factors are 1.68, 2 and 1.41. Thus, toroidal magnetic field (Bt) in D plasma was set to be 2.75 T, which is the maximum magnetic field in LHD at $R_{\text{ax}} = 3.6$ m, and Bt was set to be 1.64 T in H plasma. For the comparison of different device size, other geometrical factors and magnetic configuration factors should be adjusted [59, 60], however, the experiments in LHD were performed with the same magnetic configuration, which is an inward-shifted configuration ($R_{\text{ax}} = 3.6$ m), thus such adjustments are not necessary.

Figure 7 shows example of dimensionally similar plasma in H and D plasma. As shown in figures 7(a)–(c), normalized density and temperature profiles show excellent matching. The nondimensional parameters are almost identical in the entire region of the plasma as shown in figures 7(d)–(f).

As shown in equation (6), the obtained scaling shows ρ^{*-3} dependence indicating that global energy transport is gyro-Bohm character. On the other hand, dependences on ν^* and β are weak. In addition, the important result is that positive mass dependence co-exists in equation (6). The contradiction between gyro-Bohm scaling and non-negative ion mass dependence have been reported in many publications. However, equation (6) indicates that gyro-Bohm character and positive mass dependence are not contradictory.

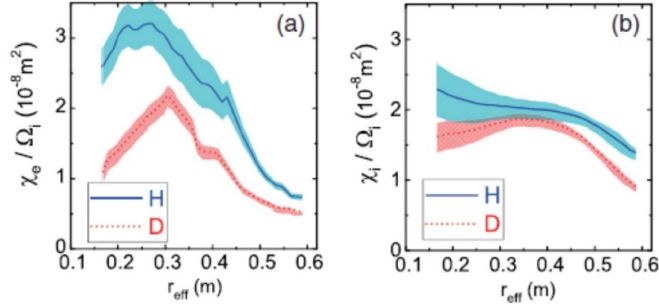


Figure 8. Comparison of the thermal diffusivity in a pair of dimensionally similar hydrogen (solid curves) and deuterium (dashed curves) plasmas shown in figure 6. Thermal diffusivity is normalized by the ion cyclotron frequency. (a) Electron thermal diffusivity and (b) ion thermal diffusivity [58]. Reprinted figure with permission from [58], Copyright (2019) by the American Physical Society.

Figure 8 shows local power balance analyses of the shots in figure 7. In figure 8, thermal conductivities are normalized by Ω_i . The normalized thermal conductivity (χ/Ω_i) is proportional to ρ^{*3} in gyro-Bohm diffusion. As shown in figure 7(d), ρ^* is identical in both H and D plasma in the entire region. Thus, if transport is purely gyro-Bohm, χ/Ω_i should be identical in H and D plasma. However, as shown in figure 8, both χ_e/Ω_i and χ_i/Ω_i are smaller in D plasma than in H plasma. The reduction is larger in the electron channel, however, the reduction is clear in the ion channel as well taking into account the uncertainty of the estimation [58]. The local analyses also show that both electron and ion transports do not have simple gyro-Bohm characteristics as well as global energy transport as shown by equation (6) [58].

Figure 9 shows the collisionality dependence of normalized thermal conductivity ratios between H and D plasma at $\rho = 2/3$. The obtained scaling of dimensionless parameters equation (6) is approximated by $\tau_E \Omega_i \propto M^{-1}$ for identical $\rho^* \nu^* \beta$, then, the following equation is obtained

$$\frac{\chi}{\Omega_i} \propto M^{-1}. \quad (7)$$

The ratio of the normalized thermal conductivity is given by the following:

$$\frac{\chi^D/\Omega_D}{\chi^H/\Omega_H} \cong \frac{M_H}{M_D} = 0.5. \quad (8)$$

As shown in figure 9(a), $\frac{\chi_e^D/\Omega_D}{\chi_e^H/\Omega_H}$ at $\rho = 2/3$ ($r_{\text{eff}} = 0.4$ m) of all the data sets is around 0.5. As shown in figure 8(a), this ratio is kept over almost the entire region of plasma. While as shown in figure 9(a), $\frac{\chi_i^D/\Omega_D}{\chi_i^H/\Omega_H}$ at $\rho = 2/3$ ($r_{\text{eff}} = 0.4$ m) becomes higher than 0.5 with increase of ν^* . However, as shown in figure 9(b), the dominant transport channel is the electron channel in the whole data set of H and most of the data set of D plasma showing $q_e/q_i > 1$. This effect is clearer in H plasma at higher ν^* . With increase of the collisionality ($\nu^* \propto n/T_e^2$), q_e/q_i decreases both in H and D plasma as shown in figure 9(b). This is due to the increase of equipartition heating power P_{ei} . As shown in

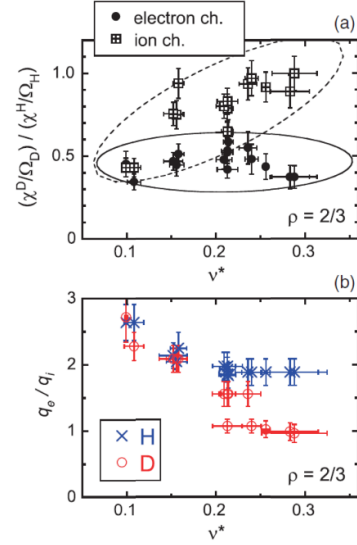


Figure 9. Comparison of the thermal transport in pairs of dimensionally similar hydrogen and deuterium plasmas. (a) The ratio of thermal diffusivity in a deuterium plasma to that in a hydrogen plasma at $\rho (= r_{\text{eff}}/a) = 2/3$ as a function of the collisionality. Closed circles and crossed squares are the electron heat loss channel and ion heat loss channel, respectively. Ellipses are 95% probability. (b) The ratio of electron heat flux to ion heat flux at $\rho = 2/3$ as a function of the collisionality. Crosses and open circles are hydrogen and deuterium plasmas, respectively [58]. Reprinted figure with permission from [58], Copyright (2019) by the American Physical Society.

equation (4), P_{ei} is proportional to n^2 , m_i^{-1} and $T_e - T_i$. The electron temperature is about twice as high as the ion temperature in the entire region of H and D plasma due to electron dominant heating of NNB. The electron density is doubled in D plasma compared to H plasma to adjust ρ^* , ν^* and β , thus, P_{ei} is higher in D plasma than in H plasma due to the n^2 dependence of P_{ei} . Thus, $\frac{\chi_i^D/\Omega_D}{\chi_i^H/\Omega_H} > 0.5$ at $\nu^* > 0.15$ does not affect the total transport and finally, local characteristics shown by equation (8) agree with global characteristics of τ_E shown by $\tau_E \Omega_i \propto M^{-1}$, which is an approximation of equation (6).

In JET ELMy H mode plasma, the main isotope effects originate from the edge pedestal [7, 18]. Since the present data set from LHD does not show clear formation of an edge pedestal, comparison should be made with JET L mode plasma [8]. In JET L mode plasmas, the values of normalized effective thermal conductivities in H and D plasmas are close, within the estimation uncertainty [8]. The difference between LHD and JET results may be due to the differences in magnetic configuration parameters or due to the differences in the plasma parameters. One of the important differences of the plasma parameters are temperature ratios (T_e/T_i). In JET L mode plasma, $T_e \approx T_i$, while in LHD, $T_e/T_i > 1$ over the entire region as shown in figures 7(a) and (b). This is because in JET, PNBs were used and PNB predominantly heated ions, while in LHD NNBs were used and NNB predominantly heated electrons. Experiments and analyses using PNBs will be performed with LHD as the next steps for a clearer understanding of the effect of temperature ratio.

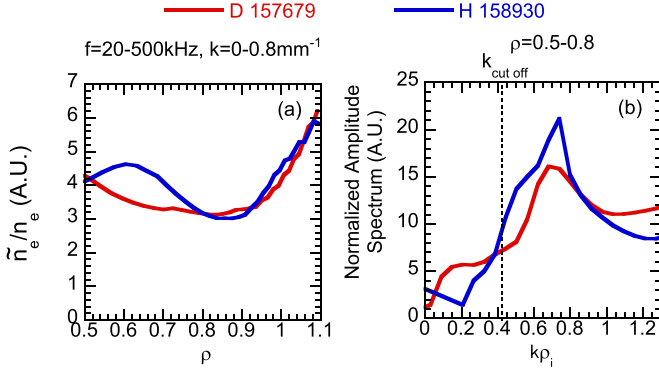


Figure 10. (a) Turbulence level and (b) wavenumber spectrum in dimensionally similar plasma measured by 2D-PCI. In (b), wavenumber is normalized by ion Larmor radius ρ_i ($= 1.7$ mm) and the spectrum amplitude is normalized by the density at $\rho = 0.5$ – 0.8 .

Figure 10 shows comparison of turbulence in dimensionally similar plasma. Three nondimensional parameters (ρ^* , ν^* and β) matched over the entire region of the plasma. The fluctuation level is higher in H plasma at about $\rho = 0.5$ – 1.0 as shown in figure 10(a). Figure 10(b) shows comparison of wavenumber spectrum at about $\rho = 0.5$ – 0.8 . In figure 10(b), the wavenumber is normalized by ρ_i , which is 1.7 mm for both cases, and spectrum amplitude is normalized by the averaged densities at about $\rho = 0.5$ – 0.8 , which are $1.6 \times 10^{19} \text{ m}^{-3}$ in H and $3 \times 10^{19} \text{ m}^{-3}$ in D plasma. The peak normalized wavenumber ($k\rho_i$) is almost identical and is ~ 0.7 . The normalized amplitude is clearly lower in D plasma around the spectrum peak. This observation qualitatively agrees with reduced transport in D plasma. It is in contrast to the observation in ECRH plasma, where peak absolute wavenumber is almost identical as shown in figure 4, but normalized wavenumber $k\rho_i$ is higher in D plasma.

4. Isotope effects of ITB plasma

The internal transport barrier (ITB) plasma is the improved confinement mode, which is observed both in a tokamak and a stellarator/heliotron [62]. The internal transport barrier is defined as a bifurcation of the flux-gradient relationship between enhanced transport and reduced transport in the internal confinement region [62]. The barriers are formed generally at $\rho = 0.2 \sim 0.7$. It is contrast to the edge transport barriers in *H* mode, where transport barriers are formed at $\rho \sim 1.0$. The formation of ITB causes steep density and/or temperature gradients due to the reduction of the local transport in the core region. In a tokamak, ITBs are formed in particle, electron, and ion energy transport simultaneously. While in LHD, an ITB is formed only in a single transport channel. For example, the particle ITB is formed with pellet injection [63, 64], the electron ITB is formed by strong central ECRH [65], and the ion ITB is formed by strong PNB heating [66]. In LHD, isotope effects were found in formation of the ITB of electron energy transport (electron-ITB) and ion energy transport (ion-ITB). In the following subsection, isotope effects in the electron and ion ITB are discussed. The role of carbon impurity on the ion

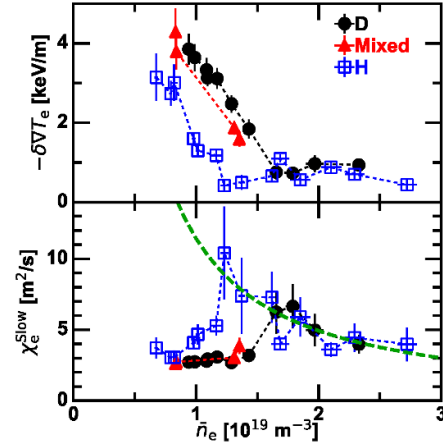


Figure 11. Dependence on line-averaged density of change of T_e gradient during ECRH modulation and thermal conductivities from local power balance analyses at $r_{\text{eff}} = 0.15$ m ($r_{\text{eff}}/a_{99} = 0.25$, a_{99} is minor radius, where 99% of kinetic electron energy is stored inside this radius). The data of H, D and H–D mixed plasma are shown. The green lines are predicted values from high density data on non-electron-ITB plasma [67]. Reproduced courtesy of IAEA. Figure adapted from [67]. Copyright (2020) IAEA.

ITB formations are also discussed in the following subsection.

4.1. Isotope effects in electron-ITB

A strong central ECRH induces a positive radial electric field in the central region. As the outer region is ion root due to equalized electron and ion temperature, thus, a negative radial electric field is formed. Then, strong Er-shear is formed between positive Er in the core region and negative Er in the outer region, and it stabilizes turbulence and reduces transport [65]. In order to investigate the isotope effects on electron-ITB, analyses of the ECRH modulation were performed [67]. Figure 11 (top) shows the change of T_e gradient between ECRH on and off timing. At lower line-averaged density, the T_e gradient increases clearly indicating the formation of electron-ITB. The increase of T_e gradient appears at higher density in D plasma than in H plasma. In the mixed H and D plasma, the electron-ITB appears at intermediate density between H and D plasma. The electron-ITB can be formed at higher density with higher concentration of deuterium [67].

In ECRH modulation, hysteresis of heat flux was found [68, 69]. The jump of the heat flux in the hysteresis is defined as δq_{jump} and the entire heat flux q_e is modeled as

$$q_e = -n_e \chi_e^{\text{slow}} \nabla T_e + \delta q_{\text{jump}}. \quad (9)$$

Equation (9) indicates that electron heat flux cannot be described by a simple diffusion model. In equation (9), χ_e^{slow} indicates slow time scale diffusivity in the modulation, and is approximated as

$$\chi_e^{\text{slow}} \sim -\frac{(\delta q_{\text{ECH}} - \delta q_{\text{jump}})}{n_e \nabla T_e}. \quad (10)$$

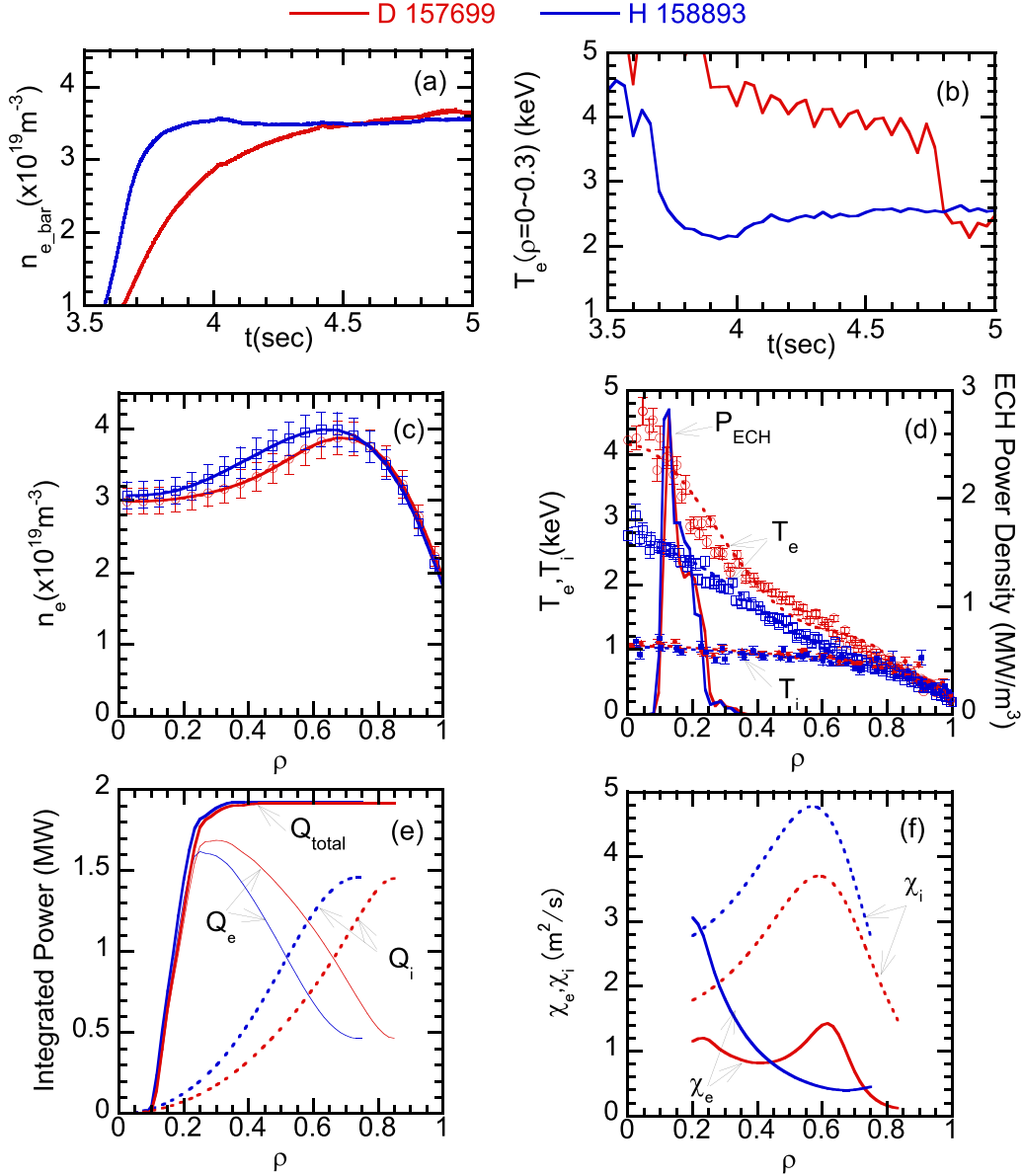


Figure 12. Comparison of e-ITB formation (a) time history of density, (b) central electron temperature, (c) n_e profiles and (d) T_e (open symbol) T_i (closed symbol) and ECRH power density (solid lines) profiles. (e) Total integrated power (Q_{total}) in thick solid lines, integrated electron power (Q_e) in thin solid lines and integrated ion power (Q_i) in dashed lines and (f) χ_e in plain lines and χ_i in dashed lines. n_e and T_e profiles are accumulated for 4.4–4.7 s. n_e profiles are from FIR interferometer [70]. T_i profiles are obtained from CXRS with short pulse (20 ms) PNB at 4.41 s. Two 154 GHz ECRH 2nd harmonic heating at 1.9 MW. In (b), the back transition takes place at $t = 4.74$ sec in shot 157699.

In equation (9), δq_{ECH} indicates the change of the heat flux due to the ECH modulation [67] and χ_e^{slow} , which corresponds to power balance χ_e [67]. As shown in figure 11 (bottom), χ_e^{slow} are almost identical at higher than $1.6 \times 10^{19} \text{ m}^{-3}$. The whole data set at this density regime follows the predicted curve from the data set in high density non electron-ITB plasma regardless of the ion species. However, at lower than $1.6 \times 10^{19} \text{ m}^{-3}$, χ_e^{slow} in mixed and D plasma clearly reduces at higher density. This result indicates that the transition to electron-ITB occurs at higher density with higher contamination of deuterium. However, no clear difference of hysteresis was found in H, mixed and D plasma [67].

Figure 12 shows the a comparison of performance of ECRH plasma in H and D plasmas. As shown in figure 12(a), the line-averaged density was identical after $t = 4.4$ sec and was $3.5 \times 10^{19} \text{ m}^{-3}$. Two 154 GHz tangentially balance injections were used. The injection power was ~ 1 MW each and total injection power was ~ 2 MW. As shown in figure 12(b), the central electron temperature was clearly higher in D plasma until $t = 4.75$ s. The electron density, temperature and ion temperature profiles are compared. For the accurate power balance analyses, n_e and T_e profiles were accumulated for approximately 4.4–4.7 s and T_i profiles were measured by CXRS with short pulse (20 ms) PNB. As shown in figure 12(c), n_e profiles are hollower in D plasma. The higher T_e are observed at $\rho < 0.8$

in D plasma and clear increase of T_e gradient appears at $\rho < 0.4$ only in D plasma indicating the formation of electron-ITB. As shown in figure 12(d), deposition profiles are identical in both cases. Power balance analyses are shown in figures 12(e) and (f). As shown in figure 12(e), the integrated power to electrons is higher in D plasma and integrated power to ions is higher in H plasma for the identical total integrated power. This is due to the higher P_{ei} in H plasma as shown in equation (4). The higher T_e in D plasma is partly due to the higher electron heating power. However, as shown in figure 12(f), χ_e is lower in D plasma than in H plasma at $\rho < 0.45$ indicating a reduction of electron transport due to the formation of an electron-ITB. Clear reduction of χ_e at higher T_e was not observed in normal confinement ECRH as shown in figure 3(d). The ion thermal conductivity is lower in D plasma than in H plasma in almost the entire region. This is due the almost identical T_i profile, while Q_i is lower in D plasma than in H plasma due to lower P_{ei} in D plasma.

4.2. Isotope effects on ion-ITB

Ion-ITB in LHD was achieved with strong ion heating. With carbon pellet injection and reduction of the edge recycling by helium glow discharge cleaning, 10 keV central ion temperature was achieved [35]. In this subsection, in order to study the isotope effects due to the difference of ion species, ion-ITBs in high purity H and D plasmas were investigated.

In an electron-ITB, the transition takes place clearly as shown in figure 12(b). On the other hand, formation of an ion-ITB is gradual. Also, ion scale turbulence changes gradually with increase of ion temperature [71, 72]. These gradual transitions make it difficult to identify the formation of the ion-ITB. Thus, in order to quantify the ion-ITB, the profile gain factor was recently defined [73]. For the definition of profile gain factor, reference T_i profiles are selected. The reference T_i profiles are low central T_i with low heating power. Then, the following ion thermal conductivity with positive temperature power index is defined:

$$\chi_i \propto T_i^\alpha, \alpha = 1 \sim 1.5. \quad (11)$$

Figure 13 shows an example to determine profile gain factor. First, in non-ITB plasma (shot 141 215, $t = 3.94$ s), the power index α is determined by using the T_i profile at $\rho > 0.6$. In figure 13, the subscript 1.0 of G indicates that $\alpha = 1.0$ in equation (11). Then, by using equation (11) with determined α , T_i profile is predicted at $\rho < 0.6$. The profile gain factor is defined from the ratio of experimental to predicted ion kinetic energy. This profile gain factor is 1.01 for the T_i profile of 141 215 $t = 3.94$ s indicating almost no gain of ion kinetic energy compared with prediction. While in the T_i profile of 141 209 $t = 4.24$ s, the profile gain factor becomes 1.47 indicating that kinetic ion energy gains are due to the ion-ITB formation. The higher profile gain factor indicates higher improvement of ion energy transport due to ion-ITB.

As shown in figure 14, the profile gain factor increases with decrease of the density. This indicates that the ion-ITB is

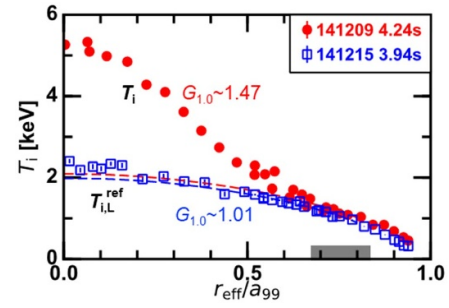


Figure 13. Comparison of T_i profiles with ion-ITB (red) and without ion-ITB (blue). Dashed lines indicates predicted T_i profiles using equation (11). $G_{1.0}$ indicates α is 1.0 from equation (11) [74]. Adapted from [74]. <https://www.nature.com/articles/s41598-019-52271-w>.

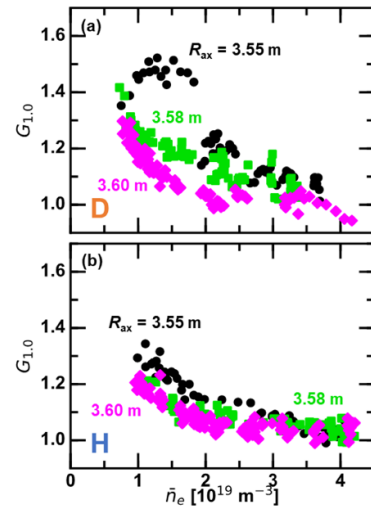


Figure 14. Comparison of profile gain factor in (a) D plasma and in (b) H plasma. The data from different magnetic axes are shown by different colors [74]. Adapted from [74]. <https://www.nature.com/articles/s41598-019-52271-w>.

formed at lower density more clearly. As shown in figure 14, the profile gain factor is systematically higher in D plasma. In figure 14, configuration dependence is also observed. Among three magnetic axes 3.55, 3.58 and 3.6 m, the profile gain factor is highest at $R_{ax} = 3.55$ m. Also, isotope effects are the strongest and the highest improvements are achieved. In all three configurations, the profile gain factor is higher in D plasma. The magnetic helical ripple is lower at more inner axis shift among these three configurations [43]. The lower magnetic helical ripple induces larger zonal flows [75, 76]. The difference of formation of zonal flow may play a role in the highest improvements at $R_{ax} = 3.55$ m.

Power balance analyses were carried out for ion-ITB plasma in H and D plasma [77]. Three NNs and two PNBs were used for the heating. Ion deposition power was adjusted to be 3 MW in both cases. Electron heating power was 5 MW in H plasma and 3 MW in D plasma. Because of the difference of the critical energy in H and D ions, simultaneous adjustment of electron and ion heating power was not technically

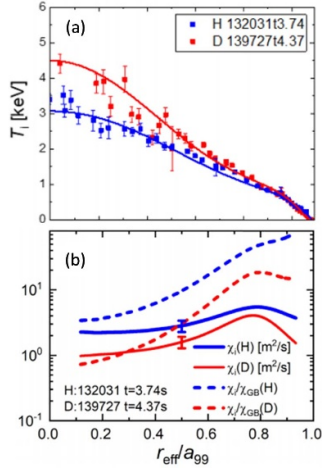


Figure 15. Profiles of (a) T_i , (b) ion thermal conductivities in ion-ITB plasma. Ion deposition power is almost identical in both discharges. The line-averaged electron density is $1.3 \times 10^{19} \text{ m}^{-3}$ in both cases. Ion deposition power is 3 MW in both cases. In (b), normalized ion thermal conductivities by gyro-Bohm diffusion, where $\chi_{GB} = \rho_i^2 v_{th}/R_{ax}$, are shown [77]. Reproduced courtesy of IAEA. Figure adapted from [77]. Copyright (2019) IAEA.

possible with H and D neutral beams. Therefore, ion deposition power was adjusted for the investigation of ion energy transport.

Figure 15 shows comparison of T_i profiles and ion thermal conductivities. As shown in figure 15(a), T_i is clearly higher in D plasma. As reported in the first publication of ion-ITB [66], the normalized thermal ion conductivities by gyro-Bohm conductivity decrease significantly toward the plasma center both in H and D plasma as shown in figure 15(b). The ion thermal conductivity without normalization is lower in D plasma than in H plasma beyond the estimation uncertainty. After normalization, the difference between H and D plasma becomes larger due to the positive ion mass dependence of χ_{GB} .

Validation between gyrokinetic analyses and experimental observation of ion transport was performed. In hydrogen ion-ITB plasma, linear [78] and nonlinear analyses [79, 80] have been performed. The nonlinear ion heat flux with non-adiabatic electron agreed with experimental values within measurement uncertainty [80]. The linear analyses [81] and nonlinear analyses with non-adiabatic electron and collisionality effects [77] were performed to for ion-ITB plasma in H and D plasma, which are shown in figure 15. Figure 16 shows linear analyses at three radial locations ($\rho = 0.3, 0.5$ and 0.6). The calculations were performed for radial wavenumber ($k_r = 0$) and finite poloidal wavenumber (k_y). The linear analyses show that dominant instability of ion scale turbulence ($k_y \rho_{ti} = 0.05\text{--}1.1$, ρ_{ti} is ion Larmor radius for H and D) is ITG at $\rho = 0.3$ and 0.5 . On the other hand, at $\rho = 0.9$, the dominant instability is TEM except $k_y \rho_{ti} < 0.25$ in D plasma. The normalized growth rate of ion scale turbulence is lower in D plasma than in H plasma in all locations and in almost the whole normalized wavenumber region. At $\rho = 0.3$ and 0.5 , the lower growth rate in D plasma is not due to the ion mass [12, 13], but is due to

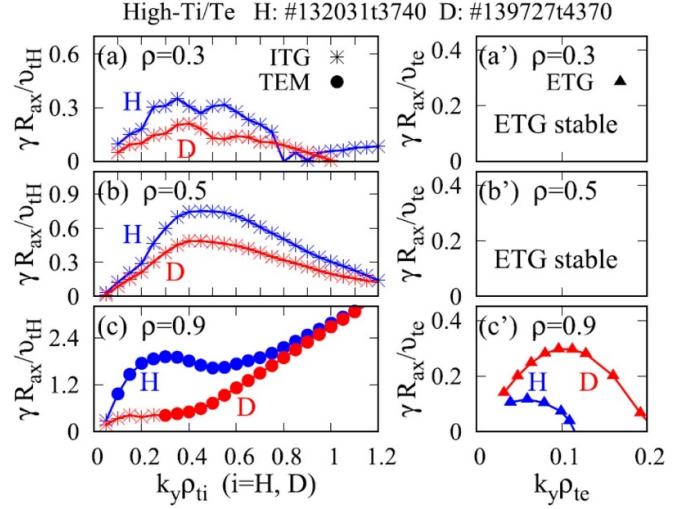


Figure 16. Linear spectrum of ion-ITB plasma in H and D plasma at (a) $\rho = 0.3$, (b) $\rho = 0.5$ and (c) $\rho = 0.9$. Most unstable mode with $k_r = 0$ are plotted. ITG is shown by asterisk, TEM by colored circle and ETG by colored triangle [81]. Reproduced from [81].

© IOP Publishing Ltd All rights reserved.

the higher T_i/T_e and hollow density profile in D plasma than in H plasma [81]. The lower growth rate in D plasma at $\rho = 0.9$ is partly due to lower density gradient and partly due to the stronger collisionality stabilization effects on TEM in D plasma [12, 13]. In electron scale turbulence, where $k_y \rho_{te}$ is approximately 0.05–0.2, k_y is poloidal wavenumber, and ρ_{te} is electron Larmor radius, ETG is stable at $\rho = 0.3$ and $\rho = 0.5$ and unstable at $\rho = 0.9$. At $\rho = 0.9$, ETG growth rate is lower in D plasma, this is partly due to lower electron temperature gradient and partly due to the lower density gradient [81].

Nonlinear simulations were carried out for H and D plasma at $\rho = 0.5$. Figure 17 shows temporal evolutions of nonlinear normalized thermal ion conductivities (χ_i/χ_{GBi} , $i = H, D$). The lower normalized ion thermal conductivities were found from the nonlinear simulations. This result is due to the larger zonal flow generation as shown in figure 17 (bottom). The zonal flow power is about 30% higher in D plasma than in H plasma. The nonlinear results account for the experimentally observed lower ion thermal conductivities qualitatively. Nonlinear χ_i/χ_{GBi} reduces by a factor of 0.36 from H plasma to D plasma. On the other hand, the experimental χ_i/χ_{GBi} reduces by a factor of 0.29 from H plasma to D plasma. The ratios of the reduction from H to D plasma are comparable in simulation and in experiment. However, absolute values do not match well. In figure 17 (top), experimental values are shown by dashed horizontal lines. Both in H and D plasma, simulation values are larger than experimental values by about a factor of 2 to 3. One of the possible disagreements is due to the strong stiffness of ion transport [80]. In LHD and tokamaks, the heat flux increases rapidly at higher than critical T_i gradients. As shown in figure 17 (top), the simulation with 20% lower normalized T_i gradient (R_{ax}/L_{Ti} , L_{Ti} ; T_i scale length) matches experimental values. The uncertainty of determination of R_{ax}/L_{Ti} is around 20%.

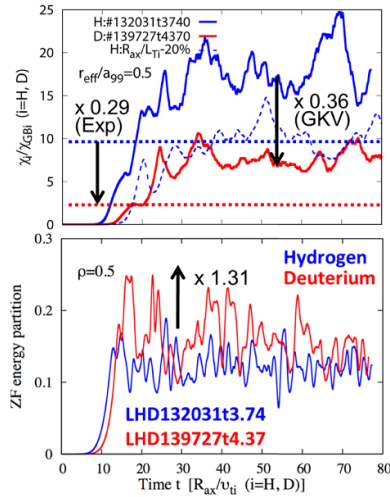


Figure 17. Temporal evolutions of nonlinear gyrokinetic (a) normalized ion heat conductivities and (b) zonal flow energy partition. In (a), experimental values are shown by thick dashed lines. The thin dashed line indicates the results of H plasma with 20% lower normalized T_i gradient [77]. Reproduced courtesy of IAEA. Figure adapted from [77]. Copyright (2019) IAEA.

Thus, results in figure 17 show agreement within experimental uncertainty.

4.3. Role of carbon impurity on ion-ITB

In LHD, high central ion temperature was achieved in PNB and NNB heated plasma with the assistance of carbon pellet injection and helium glow discharge cleaning. Higher central T_i was achieved with use of deuterium PNB. In figures 18, 16 MW H-NNB and 10 MW H-PNB were used. The shots in figure 18 were carried out in the hydrogen experimental campaign in 2013–2014. Thus, there is no deuterium in the vacuum vessel. In figures 19, 14 MW H-NNB and 17 MW D-PNB were used. The shots in figure 19 was carried out in deuterium experimental campaign in 2017. External gas fueling was not performed in either case. The fueling is due to residual helium gas after helium discharge cleaning and hydrogen and deuterium in flux from the neutralizer of NNB and PNB. In this subsection, we call the shot in figure 18 without deuterium gas H-discharge and the shots in figure 19 with deuterium gas D-discharge.

In both cases, central T_i increases after carbon pellet injection at $t = 4.6$ s. In H-discharge, central T_i reached 8 keV transiently as shown in figure 18(c). While in D-discharge, central T_i reached 9.5 keV and was maintained for around 0.2 s, as shown in figure 19(c). The injected carbon pellet is a cylindrical (1.05 mm diameter and 1.5 mm height) type. Injection speed was 190 m s^{-1} in H-discharge and 130 m s^{-1} in D-discharge. In spite of the different NB heating power and injection speed, ablation locations, which are measured by CXRS, were $r_{\text{eff}}/a_{99} = 0.8$ in both cases [82]. Thus, the different T_i observed is not due to a difference of pellet ablation.

The remarkable difference is the temporal evolutions of carbon ions. As shown in figure 18(g), the carbon peaking

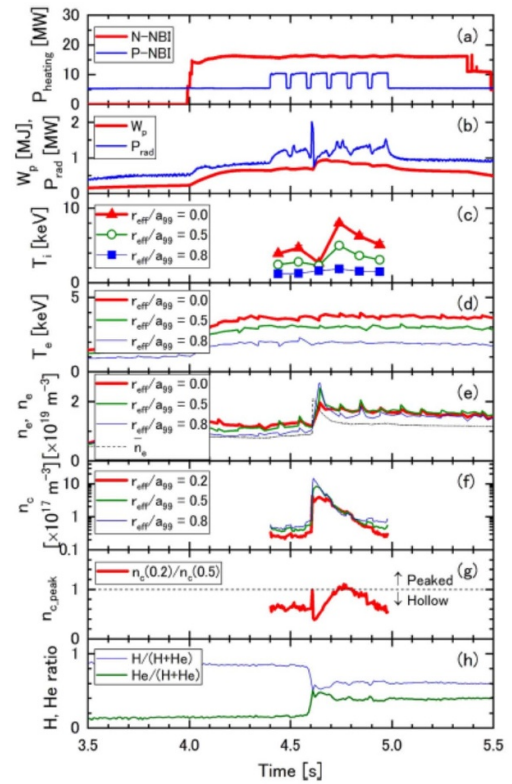


Figure 18. Time evolution in the hydrogen discharge (#123145) of (a) heating power, (b) plasma stored energy and radiated power, (c) ion temperature, (d) electron temperature, (e) electron density and line-averaged electron density, (f) carbon density, (g) peaking factor of carbon density profile, and (h) density fraction of hydrogen and helium [82]. © IOP Publishing Ltd All rights reserved.

factor, which is defined as the ratio between carbon density at $\rho = 0.2$ and 0.5 , increases up to one in H-discharges. Carbon density profiles were kept hollowed in H-discharge. On the other hand, as shown in figure 19(g), in D-discharge, the carbon peaking factor exceeded 1 and reached to 1.2. The carbon profile becomes peaked in D-discharge. In both cases, temporal evolutions of carbon profiles coincide with temporal evolutions of central T_i . This result strongly suggests that carbon profile plays a significant role to achieve higher ion temperature. It should be noted that the peaked carbon profile was achieved only in D-discharge. Thus, the observed differences of achieved central T_i and carbon profile are due to the existence of deuterium ions.

Figure 20 shows the comparison of the temporal behavior of T_i and carbon profiles [83]. Carbon density profiles are measured by CXRS by using PNB. The estimation was performed taking into account the difference of beam divergence and attenuation in hydrogen and deuterium beams [84]. As shown in figure 20(b), in H-discharge, the carbon profiles are hollow. The hollowness becomes highest at the timing of the highest T_i (4.94 s). This hollowed impurity profile is called an ‘impurity hole’ [66]. On the other hand, in D-discharge, carbon profile becomes peaked at $\rho < 0.55$. It is a strong contrast that the carbon profile is hollowed in H-discharge and peaked in D-discharge. Recent theoretical study shows that hollowed

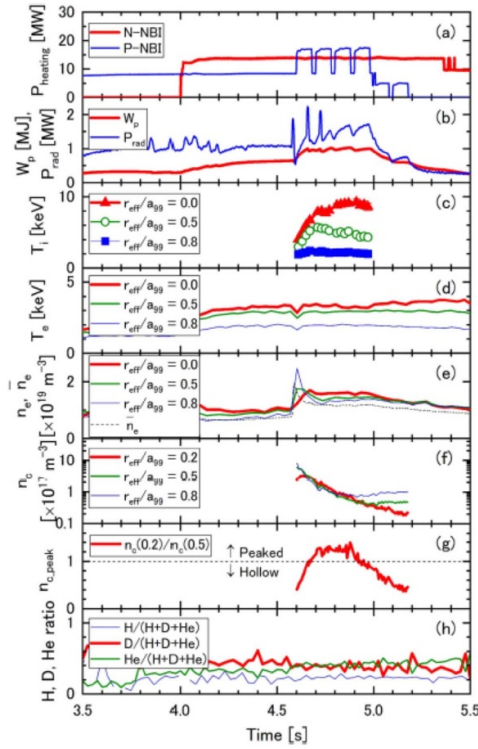


Figure 19. Time evolution in the deuterium discharge (#133707) of (a) heating power, (b) plasma stored energy and radiated power, (c) ion temperature, (d) electron temperature, (e) electron density and line-averaged electron density, (f) carbon density, (g) peaking factor of carbon density profile, and (h) density fraction of hydrogen, deuterium and helium [82]. Reproduced from [82]. © IOP Publishing Ltd All rights reserved.

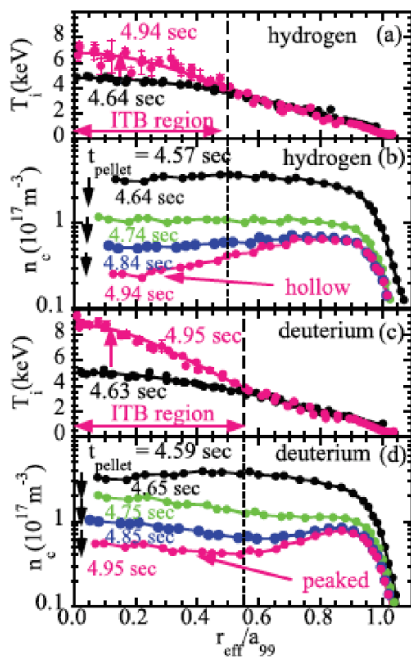


Figure 20. Temporal evolutions of ion temperature (a), (c) and carbon ion density (b), (d) in carbon pellet-assisted ion-ITB. The dashed lines indicate foot point of ion-ITB [83]. Reproduced courtesy of IAEA. Figure from [83]. Copyright (2019) IAEA.

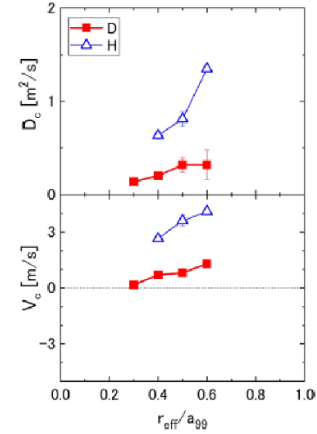


Figure 21. Diffusion coefficients and convection velocities of C6+ ions with H and D perpendicular NBI heated plasma of carbon pellet-assisted ion-ITB. Positive V_c indicates outwardly directed convection [82]. Reproduced from [82]. © IOP Publishing Ltd All rights reserved.

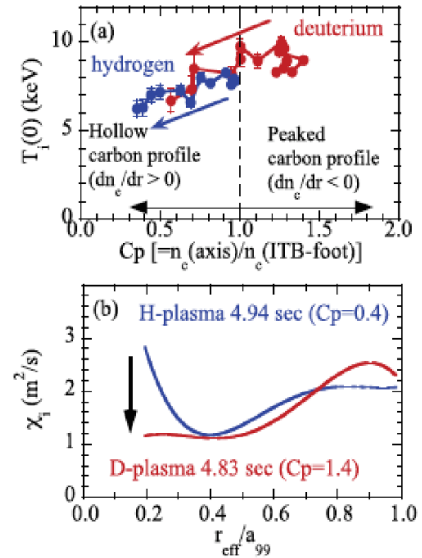


Figure 22. Relation between (a) carbon peaking factor and central ion temperature and (b) profile of χ_i in carbon pellet-assisted ion-ITB [83]. Reproduced courtesy of IAEA. Figure from [83]. Copyright (2019) IAEA.

carbon profiles destabilize ITG and enhance ion thermal transport [85, 86]. Observations in figure 20 can be possibly due to the larger stabilizing effects of ITG due to the peaked carbon profile inside the ion-ITB region.

Figure 21 shows the comparison of diffusion coefficients and convection velocities of C6+ ions injected by carbon pellet [82]. These coefficients were estimated from the relation between normalized carbon flux and normalized carbon density gradient after carbon pellet injection. As shown in figure 21, diffusion coefficients are lower and outwardly directed convection velocities are lower in D-discharge than in H-discharge. This observation results in the peaked carbon profile and its longer sustainment in D-discharge.

Figure 22(a) shows the relation between central T_i and carbon peaking factor C_p , which is defined as the ratio of carbon density at the magnetic axis to carbon density at the ITB foot point. As shown in figure 22(a), the higher central T_i is achieved at higher C_p . Also, it should be noted that the data in H-discharge and D-discharge overlap each other. This indicates that carbon profile plays a prominent role in ion transport. With deuterium contamination, peaked carbon profiles are achieved, then, the peaked carbon profile increases central T_i possibly due to the reduction of the ITG-driven turbulence. Figure 22(b) shows χ_i are clearly reduced at the location where ion-ITB is formed in D-discharge, while χ_i are comparable outside of ion-ITB.

5. Particle transport of mixed ion plasma

In the high purity H or D plasma, the spatial profiles of electron density and ion density (H or D) are identical due to the plasma quasi neutrality. In this case, diffusion coefficients and convection velocities are identical in electron and ion particle transport. However, in the mixed plasma, these coefficients of electron and ion particle transport can be different. According to the theoretical study, electron and ion transport in mixed plasma are different due to the dominant turbulence mode [87]. In the future reactor operation, the plasma will be deuterium and tritium mixed plasma. Thus, the investigations into the differences in particle transport between electron and ions are absolutely important. Such studies are possible in mixed H and D plasma with ion density measurements. In LHD, the spatial profiles of hydrogen and deuterium ions were successfully measured by using a bulk charge exchange spectroscopy [88, 89].

A new finding of the experiments in mixed plasma in LHD is the discovery of mixing and non-mixing states [90, 91]. In the mixing state, both electron and ion profile have the same shape. In the non-mixing state, electron and ion density profiles are different. The non-mixing state is clearly visible, when ion particle fueling is different in core and edge [90, 91]. Figure 23 shows mixing and non-mixing states. Three cases, which have different wall conditions, are compared. Γ_H/Γ_D is the ratio of ion influx between hydrogen and deuterium from the wall recycling and the gas fueling. This ratio was measured by passive spectroscopy with high spectrum resolution [41]. The hydrogen PNB was injected in three cases. The shape of the electron density was almost identical and hollowed in three cases as shown in figure 23(a). The hollowed density profiles in pure hydrogen plasma were well explained by the outwardly directed pinch due to the neoclassical thermo-diffusion [28]. However, H and D ion density profiles are different in three cases. In figure 23(b), the profile shape of H and D ions are almost identical and close to the electron density profile. Figure 23(b) shows the mixing state. In figure 23(c), the difference in H and D ion profiles is visible. In figure 23(d), clear differences of H and D ion profiles are found. Also, these ion density profiles are different from electron density profiles. The state in figure 23(d) is the non-mixing state. In figure 23(d), the H ion profile is peaked and D ion profiles are hollowed. The peaked H ion profile is due to low ion particle

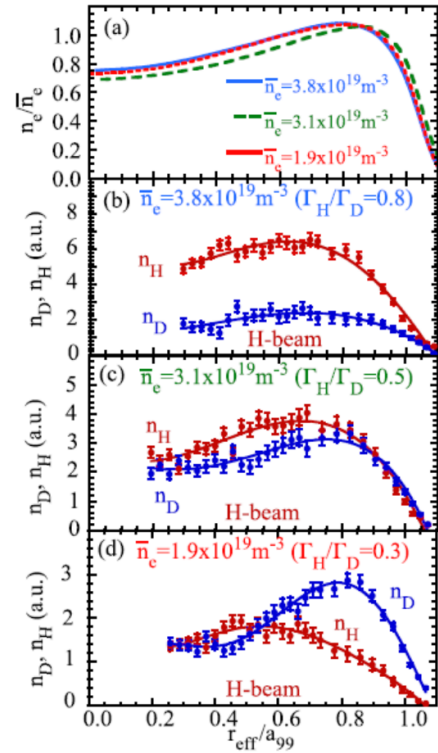


Figure 23. (a) Radial profiles of electron density and (b)–(d) radial profiles of H and D density in the plasma with H-beam fueling for the different line-averaged density and wall recycling isotope ratio of (b) 3.8×10^{19} ($\Gamma_H/\Gamma_D = 0.8$), (c) 3.1×10^{19} ($\Gamma_H/\Gamma_D = 0.5$), and (d) $1.9 \times 10^{19} \text{ m}^{-3}$ ($\Gamma_H/\Gamma_D = 0.3$) [90]. Reprinted figure with permission from [90]. Copyright (2020) by the American Physical Society.

diffusion and central particle fueling by H-PNB. The hollowed D ion profiles are due to low ion particle diffusion and deuterium edge source. Figure 23 suggests that the mixing state appears in high density and the non-mixing state appears in low density.

Further investigations were performed to understand the conditions for the mixing and non-mixing state using pellet injection. Figure 24 shows the time trace of H and D pellet injection. The pellet size and injection speed were tuned to ablate the pellet in the edge region at $r_{\text{eff}}/a_{99} \sim 0.85$ [92]. Central fueling is by H-PNB and edge fueling is deuterium by deuterium-rich wall. Figure 25 shows a comparison of H and D ion profiles before and after pellet injection. Figure 26 shows a comparison of the hydrogen ion ratio. In figure 26, a uniform hydrogen ratio indicates isotope mixing and a non-uniform profile indicates the isotope non-mixing state. Before pellet injection, H, D ion profiles and hydrogen ratios are almost identical in H and D pellet injection cases as shown in figures 25 and 26. In both cases, H ion is peaked and D ion is hollowed. Then, just after pellet injection (14 ms after in H pellet injection case and 15 ms after D pellet injection case), H and D ion profiles become hollowed in both cases as shown in figure 25. The ratio between H and D ions becomes flat in both cases as shown in figure 26. The change from non-uniform ion ratio (peaked H ion and hollowed D ion) to

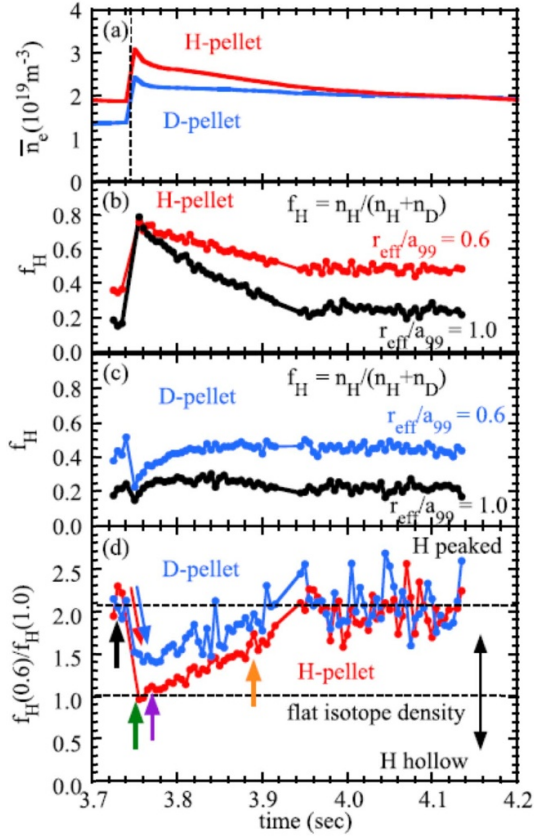


Figure 24. Time evolution of (a) line-averaged electron density, (b), (c) the fraction of hydrogen density $f_H = [n_H/(n_H + n_D)]$ at $r_{\text{eff}}/a_{99} = 0.6$ and 1.0 , respectively, and (d) the ratio of hydrogen fraction at $r_{\text{eff}}/a_{99} = 0.6$ to that at $r_{\text{eff}}/a_{99} = 1.0$ in the hydrogen and deuterium mixture plasma with hydrogen beam fueling and with hydrogen (H) pellet injection (No. 142315) or deuterium (D) pellet injection (No. 142314) [91]. Reproduced courtesy of IAEA. Figure from [91]. Copyright (2021) IAEA.

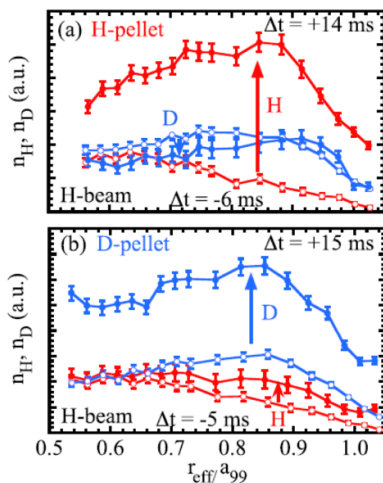


Figure 25. Radial profiles of hydrogen (H) and deuterium (D) density in the plasma with H-beam fueling before ($\Delta t < 0$) and after ($\Delta t > 0$) (a) hydrogen pellet (No. 142315) and (b) deuterium pellet (No. 142314). The peak of deposition of pellets is located at $r_{\text{eff}}/a_{99} \sim 0.9$ [90]. Reprinted figure with permission from [90]. Copyright (2020) by the American Physical Society.

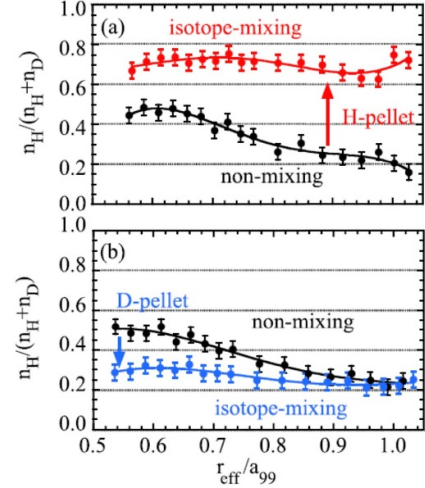


Figure 26. Radial profiles of the hydrogen isotope fraction, $n_H/(n_H + n_D)$ before and after the (a) H pellet (No. 142315) and (b) D pellet (No. 142314) [90]. Reprinted figure with permission from [90]. Copyright (2020) by the American Physical Society.

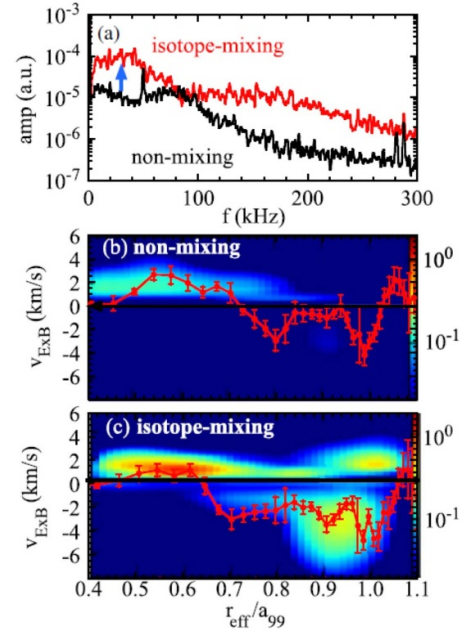


Figure 27. Line integrated density fluctuation spectrum in the non-mixing and isotope-mixing states in (a) and contour of density fluctuation in the space of the normalized minor radius and phase velocity in laboratory frame for (b) the non-mixing state and (c) isotope-mixing state (No. 142315). Radial profiles of the projection of V_{ExB} to the 2D-PCI observation plane are also plotted. The positive and negative phase velocity indicates ion and electron diamagnetic direction [90]. Reprinted figure with permission from [90]. Copyright (2020) by the American Physical Society.

uniform ion ratio (both H and D ion profiles are hollowed) indicates the transition from non-mixing to mixing state. It should be noted that the ion ratio is uniform after pellet injection, but the value of the ion ratio is different. In H-pellet injection case, edge H ion density increases, and core D ion slightly decreases. Both the peaked H ion profile and flat D ion profile

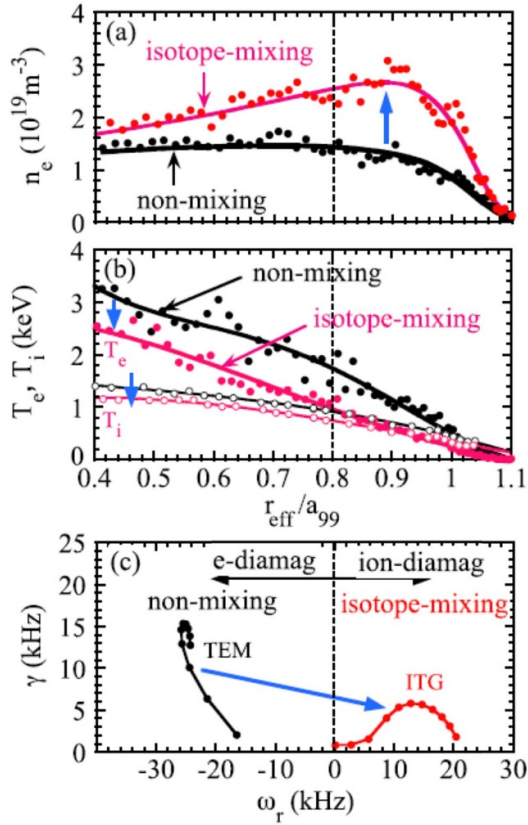


Figure 28. Radial profile of (a) the electron density and (b) the electron and ion temperature before pellet injection (non-mixing state) and after pellet injection (isotope-mixing state), and (c) the linear growth rate at $r_{\text{eff}}/a_{99} = 0.8$ for the non-mixing and isotope-mixing states calculated with GKV [90]. Reprinted figure with permission from [90], Copyright (2020) by the American Physical Society.

before pellet injection become hollowed ones after pellet injection. The majority ion is hydrogen due to H-pellet injection ($f_H = n_H/(n_H + n_D) \sim 0.7$). On the other hand, in the D pellet injection case, the D ion increases in the entire region and edge H ion increases as well. The D ion profile maintains a hollowed profile, and the H ion profiles changes from peaked profile to hollowed profile. The majority ion is deuterium due to D-pellet injection ($f_H = n_H/(n_H + n_D) \sim 0.3$). However, the mixing state does not sustain. As shown in figure 24(d), about 200 ms after pellet injection, the hydrogen peaking factor defined as $f_H(0.6)/f_H(1.0)$ returns to the initial value before pellet injection (non-mixing state). The mixing state transits back to the non-mixing state.

The physics mechanism of isotope mixing and non-mixing was also investigated. The clear difference of turbulence spatial structure was measured by 2D-PCI [48, 49]. Figure 27 shows comparison of the frequency spectrum and spatial profile of ion scale turbulence in isotope non-mixing and mixing states. The non-mixing and mixing state is before and after D pellet injection in figures 25 and 26. As shown in figure 27(a), a clear difference of frequency spectrum is found between non-mixing and mixing states. As shown in figures 27(b) and (c), the spatial structure was clearly different. In the

isotope non-mixing state (figure 27(b)), a dominant component of turbulence amplitude exists at $\rho < 0.8$. The component propagates toward the ion diamagnetic direction in laboratory frame. In the isotope mixing state (figure 27(c)), an additional turbulence component clearly appears at $\rho > 0.8$. The gyrokinetic linear analyses were performed at $\rho = 0.8$ in non-mixing and mixing state. Figure 28 shows n_e , T_e , T_i profiles and the linear spectrum. In the non-mixing state, the dominant instability is TEM and in the mixing state, the dominant instability is ITG. The key parameter is the electron density gradient. The peaked electron density gradient in the non-mixing state results in unstable TEM and the hollowed electron density gradient results in unstable ITG. The linear analyses suggests that TEM induces the non-mixing state and ITG induces the mixing state. This quantitatively agrees with theoretical considerations [87].

6. Summary

In LHD, extensive isotope experiments have been carried out. The results of the first three years of isotope experiments are reviewed. In ECRH plasma, τ_E scaling of operational parameters shows a positive ion mass dependence, which is proportional to $M^{0.27}$. The improvements of τ_E in D plasma are negligible in the low collisionality regime and become apparent in the high collisionality regime. At close to density limits, the difference becomes smaller again. In the mid collisionality regime, where isotope effects are apparent, clear reduction of the ion scale turbulence was observed suggesting reduction of turbulence-driven transport. Linear gyrokinetic analyses suggest that the hollowed density profile in D plasma stabilizes ITG, although further detailed survey is necessary considering other types of instabilities such as resistive interchange mode. In normal confinement of L mode-like NBI heated plasma, dominant heating channel was electron channel by using NNB. In the dataset, $T_e/T_i > 1$ were generally achieved in the entire region of plasma. The scaling of τ_E with operational parameters shows no mass dependence. However, normalized τ_E ($\tau_E \Omega_i$) scaling of nondimensional parameters (ρ^* , ν^* and β) shows co-existence of gyro-Bohm character ($\propto \rho^{*3}$) and positive ion mass dependence ($\propto M^{0.99}$). The normalized thermal conductivity (χ_i/Ω_i , χ_e/Ω_i) in dimensionally similar plasma of H and D plasma shows robust reduction in D plasma indicating that transport in D plasma is lower than gyro-Bohm diffusion. Degradation of ion energy transport at high collisionality in D plasma does not play a significant role in total transport, because the main transport channel is the electron channel. The turbulence in dimensionally similar plasma were compared. The turbulence level is lower in D plasma but peak wavenumber was identical. It is not clearly understood why isotope effects are more marked in ECRH plasma than in NNB heated plasma. One of the important differences is temperature ratio T_e/T_i . The temperature ratio is higher in ECRH plasma than in NNB heated plasma in the deep core region, but in toward the edge region T_e/T_i is higher in NBI heated plasma. The temperature ratio changes significantly in space in ECRH plasma, while it is almost constant in NNB plasma.

Further investigation is necessary to understand the effects of temperature ratio.

What causes the difference between a tokamak and LHD? This also is not yet clearly understood. The difference might be partly due to the plasma profile. In a tokamak, density profiles are peaked in ECRH and NBI plasma in most of the cases, while it is hollowed in LHD. In NNB plasma, the present data set from LHD are $T_e/T_i > 1$, while in most of NB heated tokamaks, T_e/T_i is close to 1 using ion heating PNB. In LHD, it is experimentally possible to obtain $T_e/T_i \sim 1$ with strong ion heating using PNB. These experiments will be done and analyzed in the near future. Also, observed differences can be caused by the difference in the magnetic configuration parameters such as q profiles, magnetic helical ripple and magnetic curvature. Further investigations are necessary to understand the magnetic configuration effects on isotope effects.

In the ITB plasma of LHD, better accessibility to electron- and ion-ITB were found in D plasma. Better accessibility and improvement of ion energy confinement are shown in the inwardly shifted configuration, where magnetic helical ripple is lower. Clearly higher central T_i was achieved in D plasma for the identical ion deposition power. Gyrokinetic simulation shows reduced growth rate and lower saturation level in D plasma. The lower saturation level in D plasma is due to the larger zonal flow generation. There are quantitative discrepancies of non-linear χ_i/χ_{GBi} and experimental χ_i/χ_{GBi} . However, the discrepancy is within the uncertainty of the normalized T_i gradient, which is 20% of the experimental value. In carbon pellet-assisted ITB, higher central T_i (~ 10 keV) was achieved in D-discharge. There is clear evidence that the carbon profile plays a role to achieve higher T_i . Peaked carbon profile helps to reduce χ_i and sustain high T_i .

In mixed plasma experiments, direct measurements of H and D ions were performed for the first time in the toroidal device. Non-mixing and mixing states are found experimentally. In the non-mixing state, ion particle diffusivity is clearly lower than electron particle diffusivity, and H and D ion density profiles are different according to source locations, while in the mixing state ion and electron particle diffusivity is comparable and shapes of H and D ion density profiles are identical, regardless of the particle source location. Gyrokinetic linear analyses show that TEM is the dominant instability in the non-mixing state and ITG in the mixing state. Measured turbulence shows different spatial structure in non-mixing and mixing states suggesting that turbulence mode is different in the two states. The mixing state is favorable for the future fusion reactor, since the He ash profile will be broadened. On the other hand, if the non-mixing state appears in the reactor, He ash accumulates in the central region and cools down the plasma. Thus, understanding the conditions for non-mixing and mixing status is absolutely essential. Our present results suggest that turbulence mode plays an important role. Also, these new findings tell us that a new approach to study of particle transport is necessary rather than estimating particle transport coefficients in the single species plasma. Presently, the experimental conditions of the mixing and non-mixing state are $n_e \sim 2 \times 10^{19} \text{ m}^{-3}$, $T_e \sim 2$ keV, while the reactor

condition is $n_e = 1 \times 10^{20} \text{ m}^{-3}$, and $T_e \sim 10$ keV. The collisionality of the present LHD experiments are about a factor of five larger than the reactor condition. Mixing and non-mixing status should be investigated at lower collisionality, which is close to reactor relevant region.

Particle transport has been extensively investigated by using density modulation experiments. The results are reported in a separate paper [33]. Generally, density profiles are hollower in D plasma both in ECRH and NBI plasma. Lower diffusion and more outward convection velocity in D plasma than in H plasma were identified. Density profiles play an important role in turbulence stabilities. A hollower profile stabilized both ITG and TEM and possibly plays a role in isotope effects.

Systematic survey of impurity transport by using a TESPEL (Tracer Encapsulated PELlet) are underway. The initial results show better confinement of vanadium ions (V^{21+}) in D plasma than in H plasma in the identical condition of ECRH plasma [93]. The detailed results will be reported in future publications.

Neoclassical transport itself does not have isotope effects. It is small in electron root and negligible in ion root. However, higher temperature in D plasma introduces enhanced neoclassical transport [27]. Observed isotope effects in LHD are prominently due to the anomalous effects.

Results from LHD show different aspects of isotope effects, which were not visible in the tokamak. Also, possible roles of turbulence on isotope effects are shown experimentally and theoretically by numerical simulations. Additional experimental data and turbulence simulations are necessary for further understanding. The isotope effects reported in this review paper are mainly about the core transport. In the next step, studies on isotope effects in the edge region should be carried out. Edge stochasticity may play a role. Such investigation will be important to clarify isotope effects in H mode [94–96] and detachment [97]. These results will contribute to the comprehensive understanding of isotope effects in toroidal devices.

Data availability statement

All data that support the findings of this study are included within the article (and any supplementary files).

Acknowledgments

This work is supported by NIFS Grants NIFS17ULHH013, NIFS18ULHH013, NIFS18KLER045, NIFS18KLPH032, NIFS18KUHL083, NIFS19KLPH038, NIFS17ULRR701, NIFS17ULRR702, NIFS17ULRR801, NIFS17ULRR808, NIFS17ULRR809, NIFS17KLPR036, NIFS16UMLG701, NIFS16ULGG801, NIFS19KLPH038, NIFS17UNTT008, NIFS17KLPR036, NIFS16KNST096, NIFS18KNXN369, NIFS16KNXN315, NIFS18KNST132, NIFS17KLPH031, NIFS17ULHH033, JSPS Grant 16H04620, JSPS Grant 17K14898, JSPS Grant 17K14899, JSPS Grant 15H02336, JSPS Grant 16H02442, JSPS Grant 17H01368, and US DOE under DE-SC0019007

Numerical simulations were performed by Plasma Simulator at NIFS, and by FX100 at Nagoya University, and supported by the NIFS collaborative Research Programs, and partly by the MEXT grant for Post K project: Development of Innovative Clean Energy, Core Design of Fusion Reactor.

ORCID iDs

K Tanaka  <https://orcid.org/0000-0002-1606-3204>

K Nagaoka  <https://orcid.org/0000-0002-5892-6047>

K Ida  <https://orcid.org/0000-0002-0585-4561>

S Satake  <https://orcid.org/0000-0002-9387-9987>

M Nakata  <https://orcid.org/0000-0003-2693-4859>

T Kinoshita  <https://orcid.org/0000-0003-3930-4434>

Y Ohtani  <https://orcid.org/0000-0003-3646-5427>

T Morisaki  <https://orcid.org/0000-0002-4428-5699>

References

- [1] Kaye S M *et al* 1997 *Nucl. Fusion* **37** 1303
- [2] Gibson A and Team J E T 1839 *Phys. Plasmas* **5** 1998
- [3] Cordey J G *et al* 1999 *Nucl. Fusion* **39** 301
- [4] Urano H *et al* 2012 *Phys. Rev. Lett.* **109** 125001
- [5] Urano H *et al* 2013 *Nucl. Fusion* **53** 083003
- [6] Schneider P A *et al* 2017 *Nucl. Fusion* **57** 066003
- [7] Maggi C F *et al* 2018 *Plasma Phys. Control. Fusion* **60** 014045
- [8] Maggi C F *et al* 2019 *Nucl. Fusion* **59** 076028
- [9] Wesson J A 1997 *Tokamaks* 2nd edn (Oxford: Clarendon)
- [10] Iter physics basis (ed) 1999 *Nucl. Fusion* **39** 2137
- [11] Garcia J *et al* 2017 *Nucl. Fusion* **57** 014007
- [12] Nakata M, Nunami M, Sugama H and Watanabe T-H 2017 *Phys. Rev. Lett.* **118** 165002
- [13] Nakata M *et al* 2016 *Plasma Phys. Control. Fusion* **58** 074008
- [14] Belli E A *et al* 2020 *Phys. Rev. Lett.* **125** 015001
- [15] Pusztai I *et al* 2011 *Phys. Plasmas* **18** 122501
- [16] Bustos A *et al* 2015 *Phys. Plasmas* **22** 012305
- [17] Mantica P *et al* 2020 *Plasma Phys. Control. Fusion* **62** 014021
- [18] Weisen H *et al* 2020 *J. Plasma Phys.* **86** 905860501
- [19] Bonanomi N *et al* 2019 *Nucl. Fusion* **59** 096030
- [20] Stroth U *et al* 1995 *Phys. Scr.* **51** 655
- [21] Yamada H *et al* 2004 *Fusion Sci. Technol.* **46** 82
- [22] Tanaka K *et al* 2016 *Plasma Phys. Control. Fusion* **58** 055011
- [23] Yamada H *et al* 2005 *Nucl. Fusion* **45** 1684
- [24] Stix T H 1972 *Plasma Phys.* **14** 367
- [25] Osakabe M 2018 *IEEE Trans. Plasma Sci.* **46** 2324
- [26] Ikeda K *et al* 2019 *Nucl. Fusion* **59** 07600
- [27] Satake S to be submitted *Plasma Fusion Res.*
- [28] Tanaka K *et al* 2010 *Fusion Sci. Technol.* **58** 70
- [29] Ohtani Y *et al* 2020 *Plasma Phys. Control. Fusion* **62** 025029
- [30] Angioni C *et al* 2009 *Plasma Phys. Control. Fusion* **51** 124017
- [31] Furno I *et al* 2003 *Phys. Plasmas* **10** 2422
- [32] Tanaka K *et al* 2019 *Nucl. Fusion* **59** 126040
- [33] Kinoshita T *et al* *Plasma Phys. Control. Fusion* to be submitted
- [34] Yoshimura Y *et al* 2018 *Plasma Phys. Control. Fusion* **60** 025012
- [35] Takahashi H *et al* 2018 *Nucl. Fusion* **58** 106028
- [36] Igami H *et al* 2019 *EPJ Web Conf.* **203** 02001
- [37] Warmer F *et al* 2018 *Nucl. Fusion* **58** 106025
- [38] Ohtani Y *et al* 2021 *Nucl. Fusion* **61** 034002
- [39] Yamada I *et al* 2010 *Fusion Sci. Technol.* **58** 345
- [40] Yoshinuma M *et al* 2010 *Fusion Sci. Technol.* **58** 37
- [41] Goto M, Sawada K and Fujimoto T 2002 *Phys. Plasmas* **9** 4316
- [42] Tsujimura T *et al* 2015 *Nucl. Fusion* **55** 12301
- [43] Murakami S *et al* 2002 *Nucl. Fusion* **42** L19–2
- [44] Yokoyama M, Watanabe K and Nakajima N 2005 *J. Plasma Fusion Res.* **81** 83
- [45] Seki R *et al* 2011 *Plasma Fusion Res.* **6** 2402081
- [46] Tanaka K *et al* 2020 *Plasma Phys. Control. Fusion* **62** 024006
- [47] Shoji M *et al* 2007 *J. Nucl. Mater.* **363–365** 827–32
- [48] Tanaka K, Michael C A, Vyacheslavov L N, Sanin A L, Kawahata K, Akiyama T, Tokuzawa T and Okajima S 2008 *Rev. Sci. Instrum.* **79** 10E702
- [49] Michael C A *et al* 2015 *Rev. Sci. Instrum.* **86** 093503
- [50] Dong J Q and Horton W 1995 *Phys. Plasmas* **2** 3412
- [51] Watanabe T-H *et al* 2006 *Nucl. Fusion* **46** 24
- [52] Nunami M, Watanabe T-H and Sugama H 2010 *Plasma Fusion Res.* **5** 016
- [53] Tokuzawa T *et al* 2021 *Rev. Sci. Instrum.* **92** 043536
- [54] Plunk G G *et al* 2019 *Phys. Rev. Lett.* **122** 035002
- [55] Shats M G *et al* 1995 *Phys. Plasmas* **2** 398
- [56] Carreras B A and Diamond P H 1989 *Phys. Fluids B* **1** 1011
- [57] Watanabe K Y, Masamune S, Takemura Y, Funaba H, Sakakibara S, Watanabe F, Tanaka K, Ohdachi S, Toi K and Narushima Y 2011 *Phys. Plasmas* **18** 056119
- [58] Yamada H *et al* 2019 *Phys. Rev. Lett.* **123** 185001
- [59] Luce T C *et al* 2008 *Plasma Phys. Control. Fusion* **50** 043001
- [60] Luce T C *et al* 2002 *Nucl. Fusion* **42** 1193
- [61] Cordey J G *et al* 2000 *Plasma Phys. Control. Fusion* **42** A127–132
- [62] Ida K *et al* 2018 *Plasma Phys. Control. Fusion* **60** 033001
- [63] Ohya N *et al* 2006 *Phys. Rev. Lett.* **97** 055002
- [64] Sakamoto R *et al* 2009 *Nucl. Fusion* **49** 085002
- [65] Yokoyama M *et al* 2007 *Nucl. Fusion* **47** 1213
- [66] Ida K *et al* 2009 *Phys. Plasmas* **16** 056111
- [67] Kobayashi T *et al* 2020 *Nucl. Fusion* **60** 076015
- [68] Inagaki S *et al* 2013 *Nucl. Fusion* **53** 113006
- [69] Itoh K, Itoh S-I, Inagaki S, Kasuya N and Fujisawa A 2016 *J. Phys. Soc. Japan* **85** 014501
- [70] Tanaka K *et al* 2008 *Plasma Fusion Res.* **3** 050
- [71] Tanaka K *et al* 2010 *Plasma Fusion Res.* **5** S2053
- [72] Tanaka K *et al* 2017 *Nucl. Fusion* **57** 116005
- [73] Kobayashi T *et al* 2019 *Plasma Phys. Control. Fusion* **61** 085005
- [74] Kobayashi T, Takahashi H, Nagaoka K, Sasaki M, Nakata M, Yokoyama M, Seki R, Yoshinuma M and Ida K 2019 *Sci. Rep.* **9** 15913
- [75] Sugama H and Watanabe T-H 2005 *Phys. Rev. Lett.* **94** 115001
- [76] Watanabe T H *et al* 2008 *Phys. Rev. Lett.* **100** 195002
- [77] Nagaoka K *et al* 2019 *Nucl. Fusion* **59** 106002
- [78] Nunami M *et al* 2011 *Plasma Fusion Res.* **6** 1403001
- [79] Nunami M, Watanabe T-H, Sugama H and Tanaka K 2012 *Phys. Plasmas* **19** 042504
- [80] Ishizawa A, Watanabe T-H, Sugama H, Nunami M, Tanaka K, Maeyama S and Nakajima N 2015 *Nucl. Fusion* **55** 043024
- [81] Nakata M, Nagaoka K, Tanaka K, Takahashi H, Nunami M, Satake S, Yokoyama M and Warmer F 2019 *Plasma Phys. Control. Fusion* **61** 014016
- [82] Mukai K *et al* 2018 *Plasma Phys. Control. Fusion* **60** 074005
- [83] Ida K *et al* 2019 *Nucl. Fusion* **59** 056029
- [84] Ida K *et al* 2019 *Plasma Fusion Res.* **14** 1402079
- [85] Kim K *et al* 2017 *Phys. Plasmas* **24** 062302
- [86] Bonanomi N *et al* 2018 *Nucl. Fusion* **58** 026028
- [87] Bourdelle C, Camenen Y, Citrin J, Marin M, Casson F J, Koechl F and Maslov M 2018 *Nucl. Fusion* **58** 076028
- [88] Yamasaki K *et al* 2018 *Plasma Fusion Res.* **13** 1202103
- [89] Ida K *et al* 2019 *Rev. Sci. Instrum.* **90** 093503
- [90] Ida K *et al* 2020 *Phys. Rev. Lett.* **124** 025002
- [91] Ida K *et al* 2021 *Nucl. Fusion* **61** 016012
- [92] Sakamoto R *et al* 2001 *Nucl. Fusion* **41** 381

- [93] Tamura N *et al* 2018 *Proc. 45th EPS Conf. on Plasma Physics* (Prague, Czech Republic, 2–6 July 2018) vol 42A (European Physical Society) p 1624
- [94] Toi K *et al* 2005 *Phys. Plasma* **12** 020701
- [95] Tanaka K *et al* 2012 *Proc. 24th IAEA Fusion Energy Conf.* (San Diego, USA, 8–13 October)
- [96] Toi K *et al* 2014 *Nucl. Fusion* **54** 033001
- [97] Kobayashi M 2019 *Nucl. Fusion* **59** 096009